The Meteoritical Society

Meteoritics & Planetary Science 50, Nr 4, 733–758 (2015)
doi: 10.1111/maps.12396

Estimation of trace element concentrations in the lunar magma ocean using mineral- and metal-silicate melt partition coefficients

Miriam SHARP[1*], Kevin RIGHTER[2], and Richard J. WALKER[1]

[1]Department of Geology, University of Maryland, College Park, Maryland 20742, USA
[2]NASA Johnson Space Center, 2101 NASA Parkway, Houston, Texas 77058, USA
[*]Corresponding author. E-mail: msharp@umd.edu

(Received 01 March 2014; revision accepted 13 October 2014)

Abstract–This study uses experimentally determined plagioclase-melt *D* values to estimate the trace element concentrations of Sr, Hf, Ga, W, Mo, Ru, Pd, Au, Ni, and Co in a crystallizing lunar magma ocean at the point of plagioclase flotation. Similarly, experimentally determined metal-silicate partition experiments combined with a composition model for the Moon are used to constrain the concentrations of W, Mo, Ru, Pd, Au, Ni, and Co in the lunar magma ocean at the time of core formation. The metal-silicate derived lunar mantle estimates are generally consistent with previous estimates for the concentration of these elements in the lunar mantle. Plagioclase-melt derived concentrations for Sr, Ga, Ru, Pd, Au, Ni, and Co are also consistent with prior estimates. Estimates for Hf, W, and Mo, however, are higher. These elements may be concentrated in the residual liquid during fractional crystallization due to their incompatibility. Alternatively, the apparent enrichment could reflect the inappropriate use of bulk anorthosite data, rather than data for plagioclase separates.

INTRODUCTION

The Moon may have formed when a large planetesimal impacted the Earth and the resulting vaporized material coalesced (Hartmann and Davis 1975; Canup and Asphaug 2001; Ćuk and Stewart 2012). The newly formed Moon would likely have been partially to completely molten, resulting in the segregation of a metallic lunar core and the formation of a silicate lunar magma ocean (LMO) (Smith et al. 1970; Wood et al. 1970). It has been argued through thermal modeling that the LMO persisted between 40 (Elkins-Tanton et al. 2011) and 200 Myr (Solomon and Longhi 1977), although about 70% of it may have rapidly crystallized within 1 Myr (Elkins-Tanton et al. 2011). Numerous studies have modeled the crystallization sequence of the putative LMO (e.g., Taylor and Jakes 1974; Snyder et al. 1992; Elkins-Tanton et al. 2011). Most models have led to the conclusion that crystallization would have begun with the precipitation of magnesian olivine followed by orthopyroxene. Plagioclase crystallization would have been a relatively late-stage product following about 75% crystallization (Snyder et al. 1992). It is commonly believed that the anorthositic crust of the Moon subsequently formed via plagioclase flotation during the latter stages of LMO crystallization, when plagioclase was present on the liquidus (e.g., Wood et al. 1970; Walker and Hays 1977; Warren 1990).

Siderophile elements are characterized by a preference for partitioning into metal relative to silicate phases. Most also behave in predictable ways in silicate systems. Consequently, these elements are important tracers for core formation as well as magma ocean processes, crust formation, and subsequent planetary accretional processes (e.g., Wade and Wood 2005; Bottke et al. 2010). The concentrations of some highly siderophile elements (HSE; including Re, Os, Ir, Ru, Pt, Rh, Pd, and Au) in the lunar mantle have mainly been estimated through extrapolations from basalt and lunar glass compositions (Warren et al. 1999; Walker et al. 2004; Day et al. 2007). Some of these studies have projected that the lunar mantle is depleted in HSE with respect to the Earth's mantle by a factor of 20 or more,

and that the HSE are in chondritic relative abundances. A similar depletion factor of 27 has been estimated for Mo (Newsom 1986), which is a moderately siderophile element (MSE; including Co, Ni, Ga, Mo, W). Tungsten appears to be less depleted with respect to the terrestrial mantle, with a depletion factor of approximately 3 (Ranen and Jacobsen 2004) or less (O'Neill 1991). Siderophile element depletion in the lunar mantle, coupled with metal-silicate partition experiments, has been interpreted to reflect the chemical fingerprint of segregation of a small lunar core and a deep magma ocean (Righter 2002).

Despite their importance, concentrations of siderophile elements in the lunar mantle remain poorly constrained, stemming from the lack of mantle rocks in the lunar sample collection. One way to obtain new information about the siderophile element composition of the LMO, during the period of plagioclase flotation, is by reverse modeling of trace element abundances present in lunar crust believed to have been produced by flotation, such as highlands anorthosites. To do this, mineral-melt partition coefficients (D) that are relevant to LMO conditions are needed.

Plagioclase-melt D values for trace elements are largely lacking for compositions, pressures, and oxygen fugacities relevant to the precipitation of plagioclase from the LMO. Consequently, here we report the results of experiments to better establish mineral/melt partition coefficients for the HSE Ru, Pd, and Au, and the MSE Ga, Mo, and W, for the minerals plagioclase, pyroxene, and olivine, under conditions relevant to latter stages of LMO crystallization. We also examine the partitioning behavior of the lithophile elements Sr and Hf in order to compare results of our new experiments with LMO-relevant prior studies that focused on lithophile elements. In order to examine possible initial siderophile element abundances in the LMO as its crystallization began, we also report results for a series of experiments that investigate metal-silicate partitioning of the MSE Co, Ni, Mo, and W under conditions relevant for lunar core segregation.

METHODS

Starting Materials

A requirement of this study was to choose one potential composition representative of a melt that would begin to crystallize An-rich plagioclase at P–T–x conditions relevant to LMO crystallization at the point of plagioclase flotation, in order to ascertain the effects of differences in pressure and oxygen fugacity on chemical partitioning behavior. The major element composition of the synthetic LMO analog selected for study was the FP0701 composition taken from Longhi (2003). This composition was chosen because it precipitates plagioclase in high abundance, along with pigeonite, at conditions appropriate for the late stages of LMO evolution. Details of the constituent oxides are listed in Table 1. The major and trace element compositions were synthesized using reagent grade oxides and carbonates. In the sample charges, individual trace elements were added in amounts approaching 1 wt% each (Table 2), in most experiments resulting in detectable concentrations of most elements in the resulting silicate phases. The mixture was ground in an agate mortar and pestle, then baked in an oven at 800 °C for 3 h to remove the carbonate from the mixture. The mixture was stored prior to experimentation in a drying oven to prevent the adsorption of water.

Table 1. Starting silicate composition.

	Longhi (2003)	w/o Al_2O_3	LPUM-B
SiO_2	46.87	54.97	60.82
TiO_2	0.56	0.66	0.20
Al_2O_3	14.35	0.00	5.17
Cr_2O_3	0.11	0.13	0.00
FeO	19.05	22.34	9.12
MnO	0.38	0.45	0.20
MgO	8.81	10.33	20.27
CaO	9.49	11.13	4.15
Na_2O	0.19	0.00	0.06
K_2O	0.04	0.00	0.00
NiO	0.00	0.00	0.00
P_2O_5	0.04	0.00	0.00
Total	99.89	100.00	100.00

Mineral-Melt Experimental Methods

The experiments were conducted using either a gas mixing furnace that allowed exploration of different fO_2 conditions, or a piston cylinder press that allowed examination of the effects of variable pressure. Both apparatuses are housed at NASA Johnson Space Center's experimental petrology laboratories.

The sample capsules for all the low-pressure experiments consisted of Al_2O_3 alumina crucibles. They were filled with approximately 200 mg of sample powder compressed to form a pellet. The sample powder for the low-pressure experiments did not contain Al_2O_3 due to the composition of the crucible—the crucible reacted with the silicate melt at the equilibration temperatures, thus providing ample Al_2O_3 for the composition. Low-pressure charges were inserted into a muffle tube furnace and held in the hotspot with an alumina rod and Pt wire. Temperature was ramped from approximately 1000 to 1400 °C over 30 min, then

Table 2. Experimental conditions.

Comp.[a]	Exp	T (°C)	P (GPa)	delta IW	log fO_2	Phases
1	4	1160	0.0001	3.5	−8.96	Gl, Ol, Cpx,
1	5	1160	0.0001	1	−11.4	Gl,Pl,Ol,Opx
2	7	1150	1	1.8	−10.2	Gl, Ol, Pyx
2	8	1150	1.5	1.8	−10.2	Gl, Pyx, Sp
2	9	1125	1	1.8	−10.2	Gl, Pl, Pyx
2	12	1125	1	1.8	−10.2	Gl, Pl, Ol, Pyx
3	13	1160	0.0001	1	−11.4	Gl, Pl, Ol, Opx
3	16	1160	0.0001	3.5	−8.96	Gl, Pl, Sp
4	19	1125	1	1.8	−10.2	Gl, Pyx, Sp
3	20	1160	0.0001	2.5	−9.96	Gl, Pl, Sp
3	21	1160	0.0001	0	−12.4	Gl, Pl, Opx
4	22	1160	0.5	1.8	−10.2	Gl, Ol, Pl
3	23	1160	0.0001	4.5	−7.96	Gl, Pl, Pyx
4	25	1140	0.7	1.8	−10.2	Gl, Pl, Pyx, Ol
4	26	1115	1.2	1.8	−10.2	Gl, Pyx, Ol, Sp
4	27	1125	1	1.8	−10.2	Gl, Pyx, Ol, Sp
4	35	1125	1	1.8	−10.2	Gl, Pl, Ol, Pyx, Sp
5	LPUMB 1	1800	1	−1.9	−8.40	Gl, Ol, Metal
5	LPUMB 2	1800	1.5	−1.5	−7.88	Gl, Ol, Metal
5	LPUMB 3	1800	2	−1.8	−8.06	Gl, Ol, Metal
5	LPUMB 4	1800	2.5	−1.4	−7.48	Gl, Ol, Metal

[a]1: 95% silicate composition (minus Al_2O_3) 5% Re, Os, Ir, Ru, Pt, Pd, Au. 2: 96% silicate composition 2% Ru, Pd, Au, 2% Sr, Ga, W, Hf, Mo. 3: 96% silicate composition (minus Al_2O_3) 2% Ru, Pd, Au 2% Sr, Ga, W, Hf, Mo. 4: 97% silicate composition; 2% Sr, Ga, Hf; 0.5% Ru, Pd, Au; 0.5% Mo, W. 5: 90% LPUMB silicate composition 10% metals: 91% Fe, 6% Ni, 1% Co, 1% W, 1% Mo.

maintained for 10 min before being cooled at a rate of 5 °C h^{-1}, to 1160 °C. The cooling rate was sufficiently slow so that large crystals could form. The final temperature was chosen such that large plagioclase grains were present, in addition to a volume of melt adequate for analysis. That temperature was then maintained for 240 h. The oxygen fugacity of individual experiments was controlled by mixing CO and CO_2 in a reference furnace at 1200 °C, where the desired electromotive force was measured using a zirconia sensor, and adjusted before introduction to the sample (Table 2). Each experiment was quenched in water upon completion of the cooling stage.

To investigate higher pressure conditions, non-end-loaded piston cylinder apparatuses were used. For experiments up to 1.5 GPa, a 13 mm core was used, whereas for 2.0 and 2.5 GPa a 10 mm core was used. The sample assembly was similar to that used by Filiberto et al. (2008). High purity graphite capsules (containing sample) and sintered MgO spacers were placed within a graphite furnace surrounded by $BaCO_3$ and Pb foil. Temperature was slowly ramped up from ambient temperature over 30 min to 1500 °C, then maintained for 1 h. The temperature was then manually ramped down at a rate of 5 °C every 5 min to the set temperature, which varied between 1115 and 1160 °C, and the charge was then left to equilibrate for 72 h. The cooling rate was again chosen to maximize crystal growth, and the final temperature was chosen to produce the desired assemblage. Estimation of oxygen fugacity of graphite capsules at high pressures was done based on use of a Co-(Co, Mg)O sliding redox equilibria sensor (Taylor et al. 1992), in experiment 27. For this experiment, a double capsule was used in which the lower capsule (closest to the thermocouple) contained the sample, and the upper capsule (still within the hot zone of the assembly) contained the sensor. Because of the physical separation in different capsules, there was no alloying between the MgO FeO, or between Ru, Au, or Pd and the Co metal, for example. The mole fraction of CoO in MgO was 0.24, corresponding to an oxygen fugacity of −10.20 (about QFM-2.1). These results are in good agreement with values measured by Righter et al. (2009) for shergottite experiments, and Martin and Righter (2013) for pyroxene-carbonate equilibrium experiments. The experiments were quenched by turning the power to the furnace off while maintaining pressure. No mineral-melt experiments were run at pressures >1.5 GPa, because plagioclase reacts with olivine at high pressures to form pyroxene and spinel (McBirney and Aoki 1973).

Metal-Silicate Experimental Methods

A second series of experiments was conducted to determine metal-silicate partitioning of Co, Ni, Mo, and

W at pressures of 1, 1.5, 2, and 2.5 GPa. These experiments were accomplished using a modified lunar primitive upper mantle (LPUM-B) composition (Longhi 2006) (Table 1). Experimental conditions are listed in Table 2. The experimental assembly was identical to the other experiments, except for the use of an MgO capsule. Oxygen fugacity in the metal-silicate experiments was estimated relative to the IW buffer using the simple approach:

$$\Delta IW = -2 * \log(X_{Feo}/X_{Fe}) \quad (1)$$

where X_{FeO} is the mole fraction of FeO from the silicate melt, and X_{Fe} is the mole fraction of Fe from the metallic phase. This calculation allows assessment of changes in D (metal/silicate) values that might be due to fO_2 variations, as well as comparison to literature data of comparable relative fO_2.

Analytical Methods

After the experiments were completed the experimental charges were submerged in epoxy, then cut, and polished for analysis. Each sample was first analyzed using the JXA-8900 SuperProbe, located at the University of Maryland, College Park, to determine major element compositions of resulting glass and minerals. The beam size was 5 μm with an accelerating voltage of 15.0 kV, a beam current of 20 nA, and counted for 60 s. Backscattered electron (BSE) images were taken at the time of electron probe micro-analysis (EPMA). Silicates were measured for major element compositions. Metals were analyzed by EPMA for Ni, Co, Mo, and W. All of the major element analyses are reported in Table 3. The compositions for each experiment are given as averages, with the number of analyses included as n. The uncertainties provided are 1σ standard deviation of the mean. Metals were analyzed by EPMA for Fe, Ni, Co, Mo, and W (Table 4). All of the elements were above the detection limits (350 ppm for Fe, 350 ppm for Ni, 300 ppm for Co, 400 ppm for Mo, 1100 ppm for W). In one glass sample, LPUMB-2, the normal analytical method did not show W above the limit of detection. We reanalyzed this glass to increase the limit of detection for W such that we increased the current to 150 nA and counted for 180 s.

The second stage of analysis utilized laser ablation using a frequency-quintupled Nd:YAG laser, operating at 213 nm, connected to an Element 2 inductively coupled plasma mass spectrometer, also at the University of Maryland, College Park. The spot size for the laser was between 10 and 60 μm, depending on the size of the experimental products. Larger spot size, 125 μm, was used for analyzing the silicate portions of the metal-silicate experiments in order to include both glass and quenched silicates. The laser repetition rate was 7 Hz. Helium was used to flush the sample chamber and to enhance sensitivity (Eggins et al. 1998). An individual analysis consisted of 20 s of background acquisition followed by active ablation for approximately 50 s. Between sample analyses, a washout time of 180 s was employed. The isotopes monitored for the metal-silicate experiments were: ^{59}Co, ^{61}Ni, ^{62}Ni, ^{97}Mo, ^{98}Mo, ^{182}W, ^{183}W, and ^{184}W. The isotopes monitored in the mineral-melt experiments were: ^{69} Ga, ^{71} Ga, ^{88}Sr, ^{97}Mo, ^{98}Mo, ^{99}Ru, ^{101}Ru, ^{105}Pd, ^{106}Pd, ^{108}Pd, ^{187}Hf, ^{182}W, ^{183}W, ^{184}W, and ^{197}Au. Multiple isotopes of non-monoisotopic elements were monitored to check for interferences from isobars.

Raw data were processed postanalysis using LAMTRACE software (Jackson 2008) coupled with major element abundances. Concentrations of Ga, Sr, Mo, Pd, Hf, W, Ni, Co, and Au were determined by comparing intensities of known concentrations of CaO or FeO in our samples, determined by EPMA, to an external reference material. Pyroxene compositions for CaO were averaged due to their irregular zoning with respect to CaO and the large spot sizes used. The NIST 610 reference glass was used as the external reference material for calculation of concentrations for these elements. Ruthenium is not present in NIST 610 in measurable quantities, so we used the IIAB iron meteorite Filomena as the external reference material, using Ga to correct for ablation yield. This resulted in calculated NIST 610 concentrations within 10% of the standard values. The Ga concentrations for our samples, determined from the comparison to NIST 610 reference material, were then used to calculate the concentration of Ru. The concentrations of CaO, 11.5 wt%, and Ga, 438 ppm, in NIST 610 that were used are from Jochum and Nohl (2008). The Ga concentration of 59 ppm for Filomena was taken from Campbell et al. (2002), and the Fe% concentration of 93.8% comes from Walker et al. (2008).

The trace element results are reported in Table 5. Most reported concentrations are averages of multiple analyses of the same phase. The uncertainty is reported as the 1σ standard deviation of the mean of multiple measurements of the same phase. When only one measurement was made, the uncertainty reported is the 1σ standard deviation, based on counting statistics. For some elements, the concentration is less than the detection limits, which is calculated by LAMTRACE if the signal was less than three times the background taken for an individual analysis. Background signals were measured for each analysis. As a result, the limit of detection varied (between approximately 0.01 and

Table 3. Microprobe analyses of glass, plagioclase, and olivine in wt%.

Experiment	*n*	SiO_2	σ	Al_2O_3	σ	FeO	σ	MgO	σ	CaO	σ	Na_2O	σ	MnO	σ	TiO_2	σ	Cr_2O_3	σ	P_2O_5	σ	Total
LPUM B1-Gl	30	39.62	0.46	3.84	0.99	12.93	0.80	41.30	2.43	3.65	0.93	0.08	0.02	0.17	0.01	0.16	0.04	0.01	0.00	0.02	0.00	101.77
LPUM B1-Ol	6	41.13	0.26	0.24	0.09	5.39	0.13	52.31	0.19	0.43	0.11	0.02	0.00	0.08	0.01	b.d.		0.01	0.01	b.d.		99.73
LPUM B2-Gl	7	45.65	1.62	13.12	1.07	16.21	0.67	9.32	0.96	13.98	0.49	0.29	0.01	0.26	0.01	0.57	0.03	b.d.		0.07	0.01	100.44
LPUM B2-Ol	6	40.56	0.05	40.56	0.05	6.89	0.23	49.40	0.16	0.35	0.05	0.01	0.00	0.10	0.01	b.d.		b.d.		0.01	0.00	97.53
LPUM B3-Gl	10	49.96	1.03	14.68	0.46	11.99	0.23	8.69	0.52	14.32	0.44	0.22	0.02	0.21	0.01	0.60	0.02	0.01	0.00	0.05	0.01	100.86
LPUM B3-Ol	9	41.19	0.14	0.08	0.01	6.75	0.11	51.48	0.24	0.23	0.01	b.d.		0.09	0.01	b.d.		b.d.		b.d.		99.89
LPUM B4-Gl	3	34.09	0.39	2.64	2.03	22.94	0.51	13.62	0.45	28.00	0.53	0.05	0.02	0.35	0.02	0.21	0.08	n.a.		0.09	0.01	98.70
LPUM B4-Ol	9	40.84	0.20	0.42	0.15	5.76	0.39	51.57	0.44	0.58	0.13	0.01	0.00	0.07	0.01	b.d.		0.01	0.01	0.01	0.00	99.47
4-Gl	9	49.62	0.10	11.94	0.04	18.66	0.07	6.19	0.02	12.51	0.03	n.a.		0.26	0.01	0.85	0.03	0.09	0.00	n.a.		100.12
4-Opx	6	53.06	0.16	1.06	0.08	17.51	0.66	22.82	0.41	4.84	0.08	n.a.		0.37	0.02	0.07	0.01	0.41	0.03	n.a.		100.14
5-Gl	5	45.75	0.12	15.82	0.06	22.75	0.06	6.91	0.03	6.18	0.09	n.a.		0.33	0.01	1.20	0.02	0.04	0.00	n.a.		98.99
5-Ol	7	35.09	0.26	0.09	0.01	34.02	0.07	30.06	0.02	0.16	0.01	n.a.		0.37	0.01	b.d.		n.a.		n.a.		99.79
5-Opx	4	49.87	0.44	4.38	0.73	21.58	0.17	22.68	0.25	0.57	0.01	n.a.		0.31	0.01	0.20	0.03	0.40	0.05	n.a.		99.99
5-Pl	12	43.80	0.14	35.62	0.23	0.73	0.10	n.a.		19.33	0.05	0.24	0.08	0.02	0.01	n.a.		n.a.		n.a.		99.75
7-Gl	3	43.18	0.03	15.20	0.03	18.60	0.03	5.37	0.03	11.10	0.03	0.59	0.02	0.31	0.01	0.72	0.01	0.02	0.02	n.a.		97.25
7-Cpx	4	50.31	0.12	5.58	0.27	17.58	0.66	17.39	0.42	8.81	1.05	n.a.		0.40	0.01	0.17	0.01	0.37	0.05	n.a.		100.62
7-Opx	6	50.00	0.40	6.00	0.70	19.98	0.21	21.16	0.29	2.11	0.08	n.a.		0.34	0.01	0.13	0.01	0.52	0.06	n.a.		100.24
8-Gl	5	42.83	8.58	15.11	3.02	17.40	3.54	3.77	0.88	9.79	2.03	0.42	0.10	0.32	0.06	0.89	0.17	0.01	0.01	n.a.		93.66
8-Cpx	6	46.32	0.77	10.03	1.04	17.57	0.38	11.80	0.93	13.10	0.46	n.a.		0.42	0.01	0.37	0.06	0.13	0.07	n.a.		99.74
8-Opx	11	47.96	0.36	8.15	0.42	22.52	0.96	18.76	0.66	1.93	0.11	n.a.		0.43	0.01	0.14	0.01	0.40	0.05	n.a.		100.28
9-Gl	4	42.00	0.43	14.16	0.10	20.19	0.27	3.54	0.06	9.67	0.06	0.48	0.02	0.43	0.02	1.10	0.01	0.02	0.01	n.a.		94.87
9-Cpx	4	50.10	0.20	5.94	0.49	18.94	1.27	18.71	1.06	6.07	0.43	n.a.		0.58	0.02	0.16	0.01	0.44	0.10	n.a.		100.93
9-Opx	2	48.97	1.16	4.66	0.03	25.06	2.30	16.82	1.00	4.25	2.38	n.a.		0.60	0.05	0.15	0.03	0.19	0.04	n.a.		100.71
9-Pl	5	44.75	0.12	34.74	0.06	0.81	0.07	n.a.		18.18	0.06	0.94	0.01	0.03	0.01	n.a.		n.a.		n.a.		99.44
12-Gl	5	44.75	0.16	14.19	0.08	18.48	0.10	3.36	0.01	9.62	0.04	0.53	0.01	0.33	0.01	1.07	0.01	b.d.		n.a.		92.34
12-Ol	8	36.45	0.25	0.06	0.01	32.54	1.47	30.25	1.21	0.22	0.00	n.a.		0.38	0.01	b.d.		n.a.		n.a.		99.90
12-Cpx	3	47.39	0.89	8.17	1.78	19.20	1.70	13.27	1.13	11.36	1.90	0.48	0.05	b.d.		b.d.		0.08	0.02	n.a.		100.36
12-Opx	5	48.95	0.68	7.00	0.96	24.72	1.16	18.20	0.89	2.03	0.16	n.a.		0.46	0.01	0.19	0.02	0.13	0.03	n.a.		101.69
12-Pl	10	44.31	0.17	35.07	0.19	0.58	0.03	n.a.		18.13	0.15	0.78	0.05	0.03	0.00	n.a.		n.a.		n.a.		99.80
13-Gl	5	44.37	0.25	15.47	0.09	26.38	0.09	5.53	0.04	5.31	0.03	0.02	0.00	0.47	0.01	1.42	0.02	b.d.		n.a.		101.39
13-Ol	2	36.30	0.02	0.04	0.00	33.22	0.81	30.87	0.66	0.14	0.01	b.d.		0.48	0.02	b.d.		b.d.		n.a.		101.05
13-Opx	5	50.46	0.59	2.20	0.30	24.49	0.89	20.99	0.46	0.59	0.05	0.01	0.00	0.44	0.01	0.29	0.06	0.08	0.03	n.a.		99.89
13-Pl	5	43.89	0.24	35.77	0.17	0.46	0.03	0.32	0.01	19.23	0.08	0.03	0.01	0.01	0.01	b.d.		0.00	0.00	n.a.		100.55
16-Gl	4	46.51	0.12	18.82	0.04	19.72	0.08	7.17	0.04	6.33	0.04	0.02	0.01	0.38	0.01	0.79	0.02	b.d.		n.a.		101.40
16-Pl	4	44.08	0.35	35.56	0.38	0.67	0.08	0.29	0.01	19.12	0.04	0.03	0.01	0.03	0.01	0.03	0.01	0.00	0.00	n.a.		100.38
17-Gl	3	46.92	1.78	15.37	0.17	10.75	0.42	7.78	0.80	6.09	0.23	0.02	0.01	0.67	0.07	2.71	0.56	b.d.		n.a.		99.52
17-Pl	5	43.59	0.24	35.12	0.09	1.28	0.04	0.30	0.01	19.21	0.04	0.02	0.00	0.03	0.01	0.01	0.01	0.00	0.00	n.a.		100.16
19-Gl	10	44.10	0.09	15.55	0.03	16.70	0.06	3.67	0.01	9.28	0.02	0.56	0.01	0.28	0.01	0.77	0.01	0.01	0.00	n.a.		95.70
19-Ol	5	35.74	0.40	0.04	0.01	36.34	1.93	27.43	1.51	0.27	0.02	b.d.		0.46	0.02	b.d.		0.02	0.01	n.a.		100.50
19-Cpx	3	47.49	0.30	7.17	1.34	19.27	1.60	15.85	1.30	9.53	1.29	0.05	0.01	0.45	0.03	0.17	0.03	0.23	0.17	n.a.		100.67
19-Opx	3	47.41	0.70	7.31	1.37	23.82	0.17	17.60	0.57	2.64	0.15	0.01	0.01	0.43	0.02	0.15	0.03	0.16	0.04	n.a.		100.10
20-Gl	5	51.28	0.17	20.21	0.10	14.10	0.07	5.14	0.05	5.28	0.02	0.01	0.00	0.35	0.01	0.90	0.02	b.d.		n.a.		99.35

Table 3. *Continued.* Microprobe analyses of glass, plagioclase, and olivine in wt%.

Experiment	*n*	SiO_2	σ	Al_2O_3	σ	FeO	σ	MgO	σ	CaO	σ	Na_2O	σ	MnO	σ	TiO_2	σ	Cr_2O_3	σ	P_2O_5	σ	Total
20-Pl	5	44.38	0.16	35.19	0.28	0.87	0.02	0.28	0.00	18.98	0.12	0.01	0.00	0.04	0.01	0.01	0.00	0.00	0.00	n.a.		100.46
21-Gl	5	44.51	0.13	15.77	0.07	25.09	0.18	6.38	0.06	5.37	0.03	0.02	0.01	0.46	0.01	1.09	0.01	0.01	0.00	n.a.		100.51
21-Opx	5	48.07	0.30	8.55	0.85	21.81	0.19	19.82	0.15	0.70	0.04	0.01	0.00	0.40	0.01	0.23	0.02	0.04	0.01	n.a.		99.79
21-Pl	5	43.88	0.08	35.51	0.14	0.48	0.02	0.33	0.01	19.35	0.05	0.05	0.00	0.03	0.01	0.01	0.01	0.00	0.00	n.a.		100.31
22-Gl	6	46.37	0.45	11.26	0.09	19.27	0.08	4.02	0.04	9.84	0.05	1.19	0.02	0.37	0.01	1.13	0.03	0.03	0.01	0.38	0.02	100.79
22-Ol	11	35.56	0.28	0.33	0.31	37.53	0.65	24.96	0.81	0.28	0.01	0.03	0.03	0.59	0.02	0.04	0.03	0.06	0.01	0.04	0.01	99.79
22-Cpx	5	49.58	0.14	3.69	0.13	14.93	0.61	14.08	0.37	14.96	1.05	0.12	0.01	0.40	0.03	0.35	0.02	0.94	0.05	0.14	0.02	100.17
22-Pl	10	45.04	0.20	32.45	0.16	0.59	0.03	0.23	0.02	16.35	0.15	1.27	0.08	0.02	0.00	0.01	0.00	0.01	0.01	0.17	0.01	99.26
23-Gl	4	44.70	0.33	13.95	0.11	21.73	0.13	6.51	0.09	5.43	0.04	0.01	0.01	0.44	0.01	1.03	0.02	0.01	0.00	0.16	0.03	99.83
23-Opx	4	46.37	0.75	9.41	1.01	20.72	0.42	22.53	0.19	0.43	0.03	0.00	0.00	0.38	0.02	0.20	0.01	0.01	0.01	n.a.		100.40
23-Pl	4	43.67	0.22	34.54	0.09	0.94	0.03	0.37	0.01	18.93	0.09	0.02	0.01	0.03	0.01	b.d.		0.01	0.01	0.14	0.05	100.06
25-Gl	5	44.74	0.14	11.71	0.12	16.47	0.11	4.44	0.06	9.51	0.04	0.79	0.02	0.37	0.01	0.82	0.04	0.02	0.01	0.61	0.01	101.34
25-Ol	3	33.37	0.36	0.03	0.01	33.48	1.27	32.15	1.53	0.00	0.00	0.01	0.00	0.56	0.02	0.01	0.01	0.52	0.04	0.03	0.02	100.24
25-Cpx	2	48.31	0.07	5.09	0.23	14.77	0.29	15.44	0.16	12.90	0.31	0.04	0.01	0.45	0.01	0.30	0.01	0.21	0.07	0.13	0.00	100.26
25-Pl	5	43.68	0.11	32.82	0.08	0.52	0.03	0.17	0.01	16.83	0.06	0.89	0.03	0.02	0.01	b.d.		0.00	0.00	0.15	0.02	101.08
26-Gl	5	41.56	0.33	13.16	0.09	15.88	0.10	4.16	0.04	9.22	0.02	0.48	0.02	0.33	0.01	0.74	0.02	0.01	0.00	0.71	0.02	98.68
26-Ol	2	33.00	0.56	0.04	0.01	35.16	1.52	30.84	1.99	0.13	0.00	0.02	0.00	0.49	b.d.	b.d.		0.06	0.06	0.03	0.02	99.88
26-Cpx	2	45.90	0.74	7.03	0.68	16.04	0.49	13.92	0.52	12.97	0.43	0.07	0.01	0.43	0.04	0.27	0.07	0.24	0.00	0.16	0.04	98.95
26-Opx	2	46.10	0.34	7.00	0.91	21.97	0.90	20.16	0.97	1.85	0.12	0.01	0.01	0.45	0.01	0.13	0.00	0.33	0.02	b.d.	0.00	98.78
27-Gl	6	44.73	0.14	15.50	0.05	16.95	0.08	3.94	0.10	9.44	0.03	0.64	0.02	0.34	0.01	0.77	0.01	0.01	0.01	0.27	0.02	97.54
27-Ol	5	35.51	0.25	0.03	0.01	36.66	1.51	26.45	1.15	0.18	0.01	0.01	0.00	0.52	0.02	b.d.		0.03	0.02	0.04	0.01	99.61
27-Cpx	9	47.29	0.43	7.78	0.48	15.08	0.38	11.93	0.32	15.92	0.41	0.07	0.01	0.43	0.02	0.45	0.04	0.09	0.05	0.10	0.01	100.17
35-Gl	8	45.96	0.33	13.80	0.08	18.11	0.20	2.35	0.02	8.63	0.04	0.76	0.06	0.34	0.01	1.33	0.03	0.01	0.00	0.44	0.02	96.10
35-Ol	7	34.12	0.38	0.05	0.02	44.15	2.14	20.70	1.82	0.22	0.03	0.00	0.00	0.65	0.03	0.03	0.01	0.02	0.01	0.06	0.01	100.20
35-Cpx	6	46.69	0.56	6.73	1.11	20.71	1.77	12.05	0.88	10.69	1.07	0.06	0.01	0.55	0.04	0.44	0.04	0.17	0.05	0.09	0.01	99.20
35-Opx	5	48.35	0.72	5.27	0.56	22.76	2.62	16.06	1.74	4.79	0.79	0.02	0.01	0.55	0.02	0.24	0.05	0.32	0.13	0.02	0.01	99.02
35-Pl	10	43.89	0.27	34.05	0.21	0.61	0.05	0.06	0.01	17.01	0.26	0.80	0.08	0.02	0.00	0.01	0.00	0.00	0.00	0.11	0.01	100.31

Uncertainties are defined as 1σ standard deviation of the mean.

Totals include several trace element oxides (Ga_2O_3, SrO, MoO_3, HfO_2, WO_3) not listed. Full analyses listed in supporting information.

Abbreviations indicate phase analyzed: Gl = glass, Ol = olivine, Cpx = clinopyroxene, Opx = orthopyroxene, Pl = plagioclase, b.d. = below detection, n.a. = not analyzed.

Table 4. Microprobe analysis for metal (wt%).

	LPUM-B 1	σ	LPUM-B 2	σ	LPUM-B 3	σ	LPUM-B 4	σ
n	6		7		5		6	
Na	0.01	0.01	0.01	0.01	0.01	0.01	0.13	0.11
Mn	b.d.		b.d.		b.d.		0.01	0.01
Mg	0.02	0.01	0.01	0.01	0.03	0.02	0.04	0.04
Ca	b.d.		b.d.		b.d.		b.d.	
Al	b.d.		b.d.		0.01	0.01	0.01	0.01
Fe	80.17	0.51	74.63	0.58	76.40	0.72	83.49	0.57
Cr	b.d.		b.d.		b.d.		b.d.	
Si	0.07		0.07	0.01	0.14	0.05	0.01	0.01
W	0.22	0.09	1.69	0.21	1.52	0.17	0.58	0.13
Hf	0.02	0.01	b.d.		0.01	0.01	0.01	0.01
Ti	b.d.		0.02	0.01	b.d.		b.d.	
Ga	0.04	0.02	0.05	0.03	0.06	0.02	0.08	0.02
P	0.02	0.01	0.03	0.01	0.11	0.03	0.02	0.01
Mo	1.97	0.50	2.71	0.18	1.90	0.26	2.35	0.34
Co	3.64	0.44	2.29	0.59	6.35	1.10	2.70	0.15
Ni	14.06	0.88	15.97	0.86	12.51	0.94	11.52	0.45
Total	100.25		97.49		99.05		100.93	

b.d. = below detection.

1 ppm). In order to make maximum *D* value estimations where no signal was measured above the background, we took the limit of detection for the individual analysis and divided by the average concentration measured in the glass for the same experiment.

RESULTS

Run Products

The minerals present in each experiment are listed in Table 2. Images of typical metal-silicate, high pressure mineral-melt, and low pressure mineral-melt run products are shown in Fig. 1. Plagioclase crystals were present in charges generally as large laths, sometimes containing glass inclusions. Pyroxenes were generally massive, 0.1–1 mm across, with irregular compositional zoning from Ca-rich (6–13 wt%) to Ca-poor (1–4 wt%) regions which did not extend to minor elements measured by EPMA. In some experiments, pyroxenes bordered the plagioclase. Olivine morphology ranged from euhedral to anhedral. Some crystals were too small to analyze by LA-ICP-MS. Spinel was observed in some experiments, but the crystals were too small to analyze by LA-ICP-MS.

The anorthite (An) content of the plagioclase was >98 for all low-pressure experiments, and ranged from 87 to 93 for high-pressure experiments (Table 3). The low-pressure experiments produced plagioclase with An contents comparable to ferroan anorthosites (e.g., Dowty et al. 1974). The An content increased with increasing MgO wt% of the surrounding melt, similar to the trend seen in Bédard (2006) (Fig. 2), which was fit to a much wider range of plagioclase and melt compositions. Although our data are offset above the Bédard (2006) best-fit trend, they are within the large range of compositional data used to calculate the Bédard (2006) trend. Calculated mineral-melt partition coefficients are listed in Table 6. Uncertainties for partition coefficients are 1σ, as propagated from the division of the trace element concentrations and their individual uncertainties.

Nuggets

Experiments run at reducing oxygen fugacities often result in HSE nugget formation (e.g., Borisov and Palme 1995; Ertel et al. 1999; Holzheid et al. 2000). It is often not clear whether the nuggets are pre-existing metal particles that were present at run conditions, or if they exsolved from silicate upon quenching (e.g., Borisov and Palme 1995; Cottrell and Walker 2006). Heterogeneous concentrations of HSE in the glass, and the increase in HSE concentrations correlating with areas of increasing nugget fractions, have been cited as reasons for favoring an interpretation that the nuggets represent pre-existing metal particles (Borisov and Palme 1995; Ertel et al. 2008). Other studies have favored an interpretation that nuggets form upon quench, based on observations that for some experiments, nugget size appears to be a function of quench rate, with faster cooling leading to smaller nuggets (e.g., Cottrell and Walker 2006). Also, in the

Table 5. Trace element concentrations in glass, plagioclase, pyroxene, and olivine in ppm.

		n	Ga	σ	Sr	σ	Hf	σ	Co	σ
LPUMB 1	Glass	4	n.a.		n.a.		n.a.		1.9E+02	1.5E+01
LPUMB 2	Glass	4	n.a.		n.a.		n.a.		4.1E+02	4.7E+01
LPUMB 3	Glass	4	n.a.		n.a.		n.a.		8.6E+02	5.5E+01
LPUMB 4	Glass	4	n.a.		n.a.		n.a.		1.0E+03	2.1E+02
Mpl 4	Glass	3	8.7E+00	1.5E-01	n.a.		n.a.		n.a.	
	Pyroxene	1	1.1E+00	*9.2E-02*	n.a.		n.a.		n.a.	
Mpl 5	Glass	1	1.2E+01	*4.6E-01*	n.a.		n.a.		n.a.	
	Olivine	1	9.6E+00	*3.3E-01*	n.a.		n.a.		n.a.	
Mpl 7	Glass	2	2.2E+03	4.5E+01	8.6E+02	4.9E+02	4.3E+03	3.7E+01	n.a.	
	Pyroxene	1	4.8E+03	*6.1E+00*	1.9E+01	*2.0E-02*	1.8E+03	*1.4E+00*	n.a.	
Mpl 8	Glass	1	2.2E+03	*3.4E+00*	2.4E+03	*2.3E+00*	4.0E+03	*3.8E+00*	n.a.	
	Pyroxene	1	4.8E+03	*4.8E+00*	1.9E+01	*8.8E-01*	1.8E+03	*4.3E+00*	n.a.	
Mpl 9	Glass	3	2.3E+03	8.6E+01	3.7E+03	3.3E+02	5.6E+03	6.4E+02	n.a.	
	Plagioclase	2	1.8E+03	2.7E+02	3.0E+03	1.0E+03	<0.55		n.a.	
Mpl 12	Glass	3	2.1E+03	9.3E+01	3.5E+03	1.3E+02	4.5E+03	1.4E+02	n.a.	
	Olivine	1	7.2E+01	*1.8E+00*	<3.09		6.9E+01	*1.4E+00*	n.a.	
Mpl 13	Glass	4	1.2E+03	8.3E+01	1.5E+03	5.4E+01	6.6E+03	1.4E+02	n.a.	
	Plagioclase	2	1.5E+03	7.1E+01	4.7E+03	7.8E+01	4.4E-01	1.7E-01	n.a.	
	Olivine	1	4.8E+02	*2.2E+00*	7.6E-01	*5.5E-02*	5.9E+02	*2.0E+00*	n.a.	
Mpl 16	Glass	4	1.1E+03	3.9E+01	1.8E+03	1.8E+01	3.5E+03	1.1E+02	n.a.	
	Plagioclase	4	1.1E+03	3.1E+01	4.1E+03	2.1E+02	8.9E-01	1.6E-01	n.a.	
Mpl 19	Glass	3	2.4E+03	4.1E+01	n.a.		3.5E+03	1.0E+02	n.a.	
	Pyroxene	1	2.0E+02	*3.0E-01*	2.3E+01	*7.0E-02*	3.0E+02	*3.3E-01*	n.a.	
Mpl 20	Glass	5	6.7E+02	3.5E+01	1.9E+03	8.3E+01	4.8E+03	1.1E+02	n.a.	
	Plagioclase	5	8.2E+02	1.7E+01	4.3E+03	1.1E+02	1.8E+00	3.3E-01	n.a.	
Mpl 21	Glass	3	9.7E+02	1.4E+02	1.7E+03	3.8E+01	6.2E+03	3.9E+02	n.a.	
	Pyroxene	4	8.2E+02	4.3E+01	4.5E+03	6.1E+01	4.2E-01	*6.1E-02*	n.a.	
Mpl 22	Glass	4	5.0E+03	1.5E+02	n.a.		n.a.		n.a.	
	Plagioclase	3	5.8E+03	1.8E+02	9.6E+03	*1.3E+01*	<4.83		n.a.	
	Olivine	1	1.6E+02	*2.6E-01*	1.5E+02	*1.6E-01*	4.4E+02	*3.8E-01*	n.a.	
Mpl 23	Glass	5	1.3E+03	4.3E+01	2.1E+03	1.7E+01	5.9E+03	5.8E+01	n.a.	
	Plagioclase	3	1.3E+03	3.7E+01	4.5E+03	2.0E+02	4.8E-01	7.3E-02	n.a.	
	Pyroxene	2	1.3E+03	8.4E+01	5.8E-01	8.5E-02	1.1E+03	1.6E+02	n.a.	
Mpl 25	Glass	4	6.0E+03	1.8E+02	6.3E+03	1.4E+02	8.1E+03	1.0E+03	n.a.	
	Plagioclase	1	7.2E+03	*1.6E+01*	1.1E+04	*1.2E+01*	<16.70		n.a.	
	Pyroxene	1	4.4E+03	*1.2E+01*	3.4E+02	*2.1E+00*	6.1E+03	*1.2E+01*	n.a.	
	Olivine	1	3.6E+01	*9.2E-01*	<9.84		5.5E+00	*3.1E-01*	n.a.	
Mpl 26	Glass	3	4.7E+03	1.4E+02	6.9E+03	*6.2E+00*	3.3E+03	1.7E+03	n.a.	
	Pyroxene	2	3.8E+03	1.5E+02	4.5E+02	8.7E+00	4.0E+03	2.6E+02	n.a.	
Mpl 27	Glass	5	2.8E+03	2.7E+01	4.6E+03	2.5E+02	5.1E+03	2.6E+02	n.a.	
	Pyroxene	2	3.9E+03	2.9E+02	5.3E+02	3.3E+01	5.2E+03	6.4E+02	n.a.	
Mpl 35	Glass	3	3.7E+03	7.4E+01	4.0E+03	2.7E+02	2.8E+03	1.4E+02	n.a.	
	Plagioclase	2	3.6E+03	1.2E+02	8.4E+03	1.6E+02	1.6E-01	*5.2E-02*	n.a.	

Uncertainties are defined as 1σ standard deviation of the mean, in cases where only one analysis was used, 1σ standard deviation according to counting statistics was used, this is signified by italics.

b.d. = below detection, when background is zero and no detection limit can be determined, n.a. = not analyzed.

experiments of Cottrell and Walker (2006), Pt concentrations within both nugget rich zones and nugget free zones were the same, indicating homogenous mixing at run conditions. Interpretation of nuggets is important because inclusion of nuggets in silicate analysis can lead to lower *D* values than if nuggets are analytically avoided. Regardless of cause, metal alloy nuggets tend to concentrate HSE, and may limit HSE abundances in the silicate phases, making silicate-melt *D* values difficult to measure.

One means of avoiding interpretive errors resulting from nugget formation is to devise experiments that minimize or eliminate nugget formation (e.g., Brenan and McDonough 2009). All of our experiments produced at least some HSE nuggets. Texturally, the nuggets observed in our runs consisted of spherical globules that often

Ni	σ	Mo	σ	W	σ	Ru	σ	Pd	σ	Au	σ
8.4E+01	7.0E+00	1.9E+01	7.0E+00	9.5E+02	1.0E+02						
2.0E+02	4.2E+01	1.1E+01	6.0E+00	7.0E+02	1.6E+02						
2.4E+02	2.7E+01	8.0E+00	1.0E+00	3.6E+02	2.9E+01						
8.7E+02	2.1E+02	9.9E+01	4.0E+01	4.4E+03	7.1E+02						
n.a.		n.a.		n.a.				8.0E-03	*2.5E-03*	1.9E-01	4.1E-03
n.a.		n.a.		n.a.				<0.03		<0.18	
n.a.		n.a.		n.a.				1.7E-02	*5.5E-03*	<0.31	
n.a.		n.a.		n.a.				<0.05		<0.18	
n.a.		2.0E+03	2.4E+01	4.1E+03	5.4E+01	5.6E-02	1.0E-03	3.0E-02	*3.0E-03*	9.2E-02	*7.1E-03*
n.a.		1.4E+02	*3.6E-01*	<15.41		b.d.		<0.14		<0.76	
n.a.		3.0E+03	*7.5E+00*	4.7E+03	*4.4E+00*	3.7E-02	*1.5E-02*	2.5E-02	*3.6E-03*	<0.17	
n.a.		1.4E+02	*2.0E+00*	<15.41		b.d.		<0.14		<0.76	
n.a.		1.8E+03	8.4E+00	6.2E+03	3.9E+02	4.1E-02	1.2E-02	1.9E-02	*3.7E-03*	<0.12	
n.a.		<1.38		6.8E-02	*8.3E-03*	3.5E-02	*2.5E-02*	<0.05		<0.16	
n.a.		2.1E+03	1.4E+02	6.2E+03	3.5E+02	1.2E-02	3.9E-03	3.3E-02	3.5E-03	<0.11	
n.a.		2.4E+01	*2.1E+00*	6.9E-02	*4.9E-02*	b.d.		<0.15		<0.72	
n.a.		1.8E+03	6.7E+01	6.7E+03	1.4E+02	<0.21		<0.05		<0.35	
n.a.		1.9E-01	1.1E-01	1.6E-01	6.5E-02	<1.21		<0.16		<0.66	
n.a.		6.4E+01	*1.6E+00*	5.4E+00	*2.1E-01*	<0.26		<0.08		<0.29	
n.a.		2.6E+03	7.7E+01	3.9E+03	8.9E+01	<0.21		1.2E-01	3.5E-03	<0.20	
n.a.		4.9E-01	6.0E-02	2.7E-01	3.4E-02	<0.42		<0.08		<0.53	
n.a.		1.1E+03	1.3E+01	2.8E+03	3.8E+01	4.6E-02	1.0E-02	2.9E-02	1.3E-03	1.1E-01	*9.7E-03*
n.a.		4.4E+00	*8.8E-02*	2.0E-02	*2.9E-03*	9.2E-04	*6.5E-04*	1.1E-03	*2.7E-04*	<0.01	
n.a.		2.6E+03	1.6E+02	4.7E+03	1.7E+02	5.6E-02	2.8E-03	7.2E-01	1.2E-01	2.5E-01	4.3E-02
n.a.		5.4E-01	5.3E-02	6.7E-01	1.1E-01	7.1E-02	1.7E-02	4.1E-01	6.1E-02	<0.28	
n.a.		6.9E+02	4.8E+02	5.9E+03	1.0E+02	9.1E-01	*7.1E-02*	5.4E-02	2.2E-02	2.1E-01	5.0E-02
n.a.		6.8E-01	1.6E-01	<0.61		3.0E-01	1.4E-01	1.6E-02	*4.8E-03*	<0.28	
n.a.		9.2E+02	2.9E+01	5.3E+03	2.6E+02	4.9E-02	1.4E-02	b.d.		1.6E-01	2.4E-02
n.a.		<1.31		<0.83		8.7E-02	3.3E-03	b.d.		<0.18	
n.a.		3.0E+01	*2.2E-01*	2.0E+02	*2.9E-01*	b.d.		b.d.		<0.01	
n.a.		4.4E+03	4.3E+01	5.9E+03	6.3E+01	1.3E-01	7.2E-02	1.6E-01	2.6E-02	1.4E-01	*1.5E-02*
n.a.		1.8E+00	*2.7E-01*	8.9E-01	6.3E-01	7.3E-02	2.5E-02	1.8E-01	1.3E-01	<0.21	
n.a.		2.1E+00	2.0E-02	3.4E-01	5.5E-02	7.3E-02	2.1E-02	<0.04		<0.23	
n.a.		1.9E+03	3.5E+01	4.6E+03	1.3E+02	7.9E-02	5.3E-02	3.0E-02	*4.4E-03*	1.6E-01	*1.4E-02*
n.a.		<2.93		<2.20		1.8E-01	*8.1E-02*	<0.57		<0.86	
n.a.		1.7E+02	*4.6E+00*	5.7E-01	*1.3E-01*	b.d.		1.0E-02	*5.7E-03*	<0.66	
n.a.		3.3E+00	*5.4E-01*	b.d.		8.1E-02	*4.7E-02*	b.d.		<0.98	
n.a.		2.2E+03	4.8E+01	3.7E+03	1.2E+01	8.6E-02	5.7E-03	2.4E-02	4.2E-03	1.2E-01	*8.7E-03*
n.a.		6.8E+01	6.4E+00	6.1E-01	4.7E-01	2.2E-01	1.2E-01	3.0E-03	*1.1E-03*	<0.59	
n.a.		1.3E+03	2.7E+01	2.9E+03	6.2E+01	4.8E-02	8.0E-03	6.1E-02	9.6E-03	<0.17	
n.a.		7.4E+01	5.2E+00	2.5E+00	1.9E+00	2.2E-02	1.8E-03	8.5E-02	*1.4E-02*	<0.66	
n.a.		8.4E+02	2.1E+01	5.6E+03	6.6E+01	5.3E-02	1.3E-02	2.1E-02	*4.2E-03*	<0.19	
n.a.		1.7E-01	*1.2E-01*	4.0E-02	*2.8E-02*	5.1E-02	1.3E-02	5.8E-03	*2.1E-03*	<0.57	

contained two immiscible phases. One phase was rich in Au and Pd, and the other was Ru rich. These two phases were always present, under all run conditions. In the first low-pressure experiments conducted (#4–5), HSE nuggets were small and dispersed throughout the samples in both glass and mineral phases. We then reduced the number of HSE included in the rest of the experiments (#7–35) to reduce the likelihood of forming nuggets. We focused on Pd and Au as these do not tend to form nuggets and have higher silicate-melt solubilities than other HSE (Borisov and Palme 1996). We also include Ru as it has relatively high solubility in silicate melt at oxidizing conditions (Borisov and Nactweyh 1998). The change in composition produced results where the nuggets were larger and more concentrated at the tops of the sample charges, with the majority of the sample charge nugget

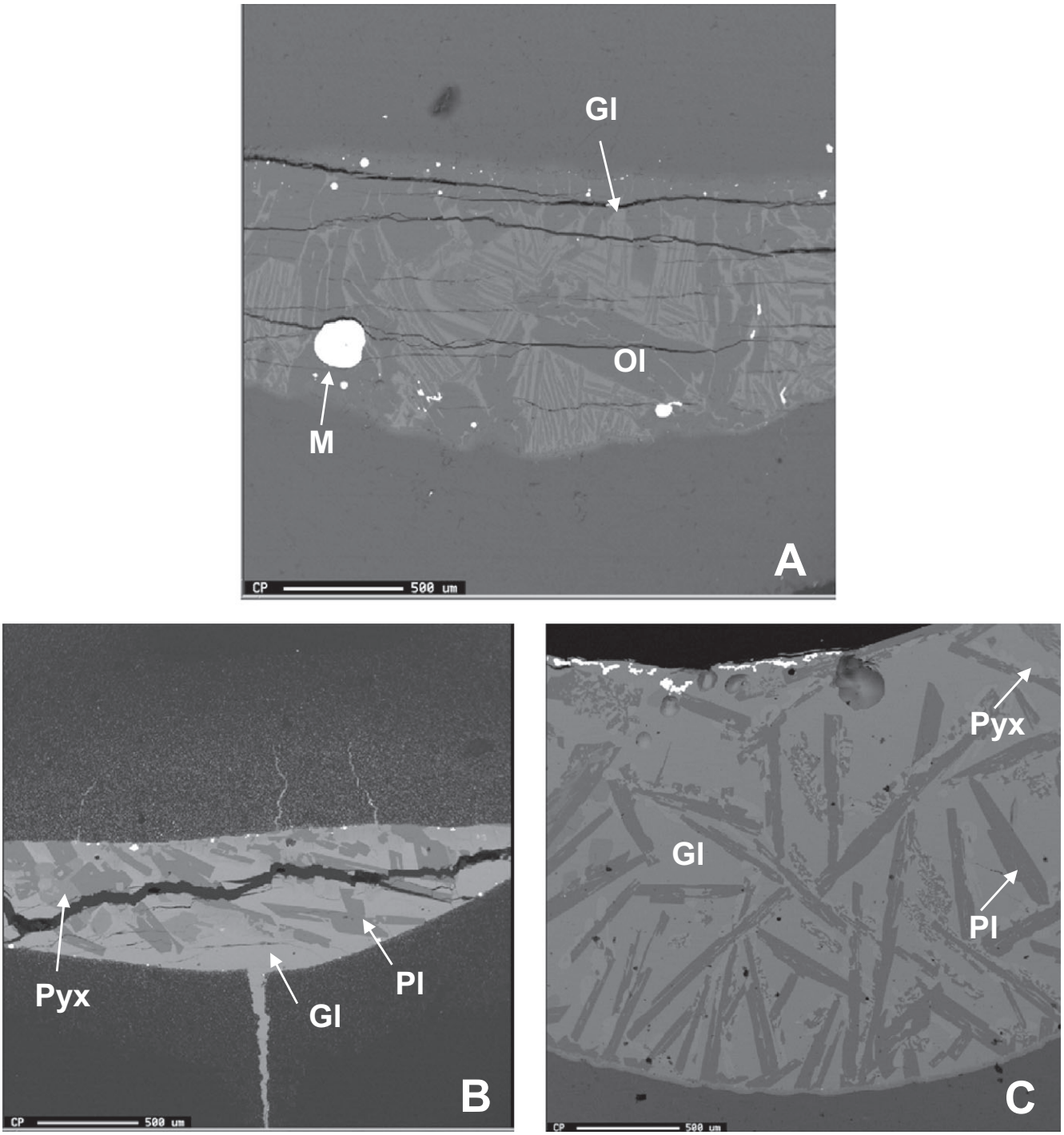

Fig. 1. This figure shows the typical textures displayed in each of the types of experiments. The top panel A is the metal-silicate experiment (LPUMB-2). Panel B is the high-pressure mineral-melt texture (#22). Panel C is the low-pressure mineral-melt texture (#5). Phases are labeled as Ol-olivine, Pl-plagioclase, Pyx-pyroxene, M-metal, and Gl-silicate glass.

free. The high-pressure experiments generally had a few large nuggets, with the majority of the phases nugget free. Because of the irregular distribution of nuggets, we assume that they were present at high temperature and avoided them in analyses.

Equilibrium

The major element behavior of Fe and Mg in olivine and Ca and Na in plagioclase can be used to indicate whether an experiment reached equilibration.

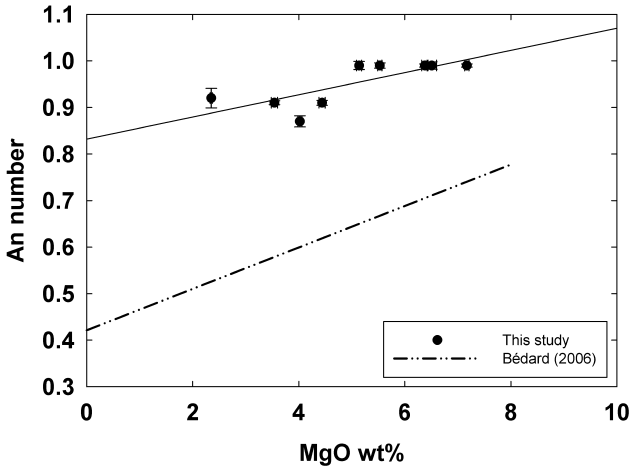

Fig. 2. MgO wt% of the melt versus An number of plagioclase. In comparison with Bédard (2006), our samples plot above the trend of that study. We do see the same increasing An content with increasing MgO wt%.

The average exchange coefficient (K_D) for Fe-Mg for olivine-melt was 0.27 ± 0.03, which overlaps with the value 0.30 ± 0.03 from Roeder and Emslie (1970) for olivine in basaltic melts. Another way we assessed the equilibrium was to estimate the temperature of the experiment using the plagioclase-liquid thermometer of Putirka (2005) and comparing it to our experimental temperatures. The average difference between the two temperatures was only 4.8%. The homogeneity of major elements within phases was determined via EPMA. Of the experimental products, only pyroxene showed any obvious zonation, in some charges varying from clinopyroxene to orthopyroxene in the same crystals.

Trace element homogeneity was monitored by examining ablation profiles as a function of time. Only analyses that yielded stable signals, and that were unaffected by spikes in signal caused by nugget ablation are considered. The HSE were generally not present in measurable amounts in either glass or mineral fractions; however, a few samples had HSE above detection limits in some phases. In these cases, the time-resolved signals were stable. Examples of a clean glass run and one with a metal alloy spike can be found in supporting information. We observed no trace element abundance zonation within any given mineral during these runs, indicating that kinetic effects were minimal.

We can also compare our measured values to those reported in previous solubility studies. For example, Borisov and Palme (1996) equilibrated basaltic silicate melts with Au-Pd alloys and reported concentrations of 0.5–1.0 ppm Pd and 0.06–0.08 ppm Au. Although these values differ somewhat from concentrations of 0.002–0.06 ppm Pd and 0.092–0.25 ppm Au in our melts, our melts equilibrated with alloys containing much lower Pd and Au contents (Table 5). The concentrations are broadly consistent with the levels measured in previous studies. The basalt compositions were somewhat different so close agreement with the prior experiment was unlikely. For Ru, Laurenz et al. (2013) measured 0.045–0.14 ppm Ru in basaltic melts equilibrated with Ru metal at fO_2 near FMQ-2. These values are similar to ours obtained for experiments run with comparable fO_2 and pressure in which we measured 0.012–0.086 ppm Ru in melts equilibrated with metallic alloys containing less Ru than the study of Laurenz et al. (2013) (Table 5). These comparisons indicate that the melts attained levels of Ru, Pd, and Au that are consistent with equilibrium and do not reflect interference from micro-nuggets of HSE metals seen in previous studies.

Metal-Silicate Partitioning

Major and trace element data for metal-silicate experiments are included in Tables 3 and 4, respectively. Calculated D values are reported in Table 6. The silicate portions of all run products consisted entirely of glass and olivine. Olivine grains were mainly large, euhedral crystals, but some were smaller and more skeletal in shape (Fig. 1). We focused on areas with coexisting glass and olivine that appeared quenched. Large laser spot sizes (60 μm) were used to obtain the average trace element composition of the silicate. Metal-silicate D values range from 130 to 440 for Ni, from 30 to 70 for Co, and from 230 to 1200 for Mo. The metal-silicate D values for W range from 0.55 to 40, with only one experiment resulting in a D value for $W < 1$.

The new metal-silicate D values for Co, Ni, Mo, and W overlap with results from previous studies that examined partitioning at pressures <5 GPa (Table 7). We observed no pressure-dependent changes in the metal-silicate D value for any of the elements examined. By contrast, oxygen fugacity and metal-silicate D values are negatively correlated for all elements examined (Fig. 3), although trends for Ni and Co are better than those for Mo and W. These results are generally consistent with results from Righter (2011).

Silicate Mineral-Melt Partitioning

Partitioning of Hf and Sr

Major and trace element data for mineral-silicate experiments are provided in Tables 3 and 4, respectively. Calculated D values are reported in Table 6. Plagioclase-melt D values for Hf range from 8×10^{-5} to 3×10^{-4}. Pyroxene-melt and olivine-melt D values for Hf range from 0.08 to 1.2 and 6×10^{-4} to 0.08, respectively. There is a modest positive correlation

Table 6. *D* values for metal-silicate and mineral-silicate experiments.

	Ga	σ	Sr	σ	Hf	σ	Mo	σ
Metal								
LPUM B1							1.0E+03	9.4E+01
LPUM B2							2.5E+03	3.8E+02
LPUM B3							2.4E+03	2.7E+02
LPUM B4							2.4E+02	1.0E+02
Plagioclase								
Mpl 9	7.7E-01	1.2E-01	8.1E-01	2.9E-01				
Mpl 13	1.2E+00	9.9E-02	3.1E+00	1.2E-01	6.5E-05	2.5E-05	1.1E-04	6.1E-05
Mpl 16	9.6E-01	4.4E-02	2.3E+00	1.2E-01	2.6E-04	4.7E-05	1.8E-04	2.4E-05
Mpl 20	1.2E+00	6.9E-02	2.3E+00	1.2E-01	3.7E-04	7.0E-05	2.0E-04	2.4E-05
Mpl 21	8.5E-01	1.3E-01	2.7E+00	7.3E-02	6.8E-05	1.1E-05	7.7E-04	4.6E-04
Mpl 22	1.1E+00	5.0E-02						
Mpl23	1.1E+00	4.6E-02	2.1E+00	9.9E-02	8.0E-05	1.2E-05	4.2E-04	6.1E-05
Mpl 25	1.2E+00	3.6E-02	1.7E+00	3.7E-02				
Mpl 35	1.0E+00	3.8E-02	2.1E+00	1.5E-01	5.9E-05	1.9E-05	2.0E-04	1.4E-04
Pyroxene								
Mpl 4	1.3E-01	1.1E-02						
Mpl 7	2.2E+00	4.6E-02	2.2E-02	1.2E-02	4.1E-01	3.5E-03	0.071	0.001
Mpl 8	1.1E+00	2.7E-03	8.0E-02	3.7E-04	6.7E-01	1.3E-03	0.037	0.001
Mpl 19	8.2E-02	1.4E-03			8.6E-02	2.5E-03	3.9E-03	8.8E-05
Mpl 23	1.0E+00	7.4E-02	2.7E-04	4.1E-05	1.9E-01	2.7E-02	4.7E-04	6.4E-06
Mpl 25	7.3E-01	2.2E-02	5.3E-02	1.2E-03	7.5E-01	9.3E-02	9.3E-02	3.0E-03
Mpl 26	8.2E-01	4.0E-02	6.5E-02	1.3E-03	1.2E+00	6.3E-01	3.1E-02	2.9E-03
Mpl 27	1.4E+00	1.1E-01	1.2E-01	9.6E-03	1.0E+00	1.4E-01	5.6E-02	4.1E-03
Olivine								
Mpl 5	8.3E-01	4.3E-02						
Mpl 12	3.5E-02	1.8E-03			1.5E-02	5.8E-04	1.1E-02	1.3E-03
Mpl 13	3.8E-01	2.6E-02	4.9E-04	4.0E-05	8.9E-02	1.9E-03	3.6E-02	1.6E-03
Mpl 22	3.1E-02	9.4E-04					3.2E-02	1.1E-03
Mpl 25	6.0E-03	2.4E-04			6.8E-04	9.2E-05	1.8E-03	2.9E-04

Note. Italics denote upper limit.

between plagioclase-melt *D* values for Hf, and the SiO_2 content of the melt (Fig. 4a). The slope of the trend is similar to that reported in Bédard (2006); however, our results are offset to lower *D* values (Fig. 4a). This may be due to compositional differences, as our melt had lower SiO_2 contents than most of the data used for the Bédard (2006) best-fit trend.

Our plagioclase-melt *D* values for Hf are consistent with the extreme incompatibility noted by Righter and Shearer (2003) and Shearer and Righter (2003). Most experimental determinations of pyroxene-melt *D* values for Hf are <1, consistent with most of our results (Klemme et al. 2006; Hart and Dunn 1993). However, two of our experiments yielded *D* values >1. The higher *D* values are consistent with the results of Bennett et al. (2004) for synthetic basalt, which reported clinopyroxene-melt *D* values that range to 1.9. The range of olivine-melt *D* values for Hf obtained here is wider than previously reported (Tables 6 and 7) (e.g., Adam and Green 2006).

Individual plagioclase-melt *D* values for Sr range from 0.8 to 3.0 and are generally consistent with the absolute range reported by prior studies (Drake and Weill 1975; Bindeman and Davis 2000). Of note, one experiment resulted in a *D* value less than 1 (see Table 7 for literature ranges for *D* values for all elements examined). Consistent with previous studies, we found no pressure dependence for Sr partitioning into plagioclase (Blundy and Wood 1991; Taura et al. 1998). By contrast, our results do not plot within uncertainties of the An content versus *D* value trends of Blundy and Wood (1991) and Bédard (2006) (Fig. 4b). In both of these studies, not as many data points were used in the trend calculations at An contents >0.95 as there were at lower An contents. The scatter of our data about the trends of Blundy and Wood (1991) and Bédard (2006) is of the same magnitude as displayed by both natural and experimental data at lower An contents (Bédard 2006).

The pyroxene-melt *D* values for Sr range from of 2×10^{-4} to 0.1, and are negatively correlated with MgO content in the melt (Fig. 4c). Strontium was also strongly incompatible with olivine. Although the Sr content we obtained was sufficiently high to measure in

W	σ	Ru	σ	Pd	σ	Au	Co	σ	Ni	σ
2.3E+00	9.8E-01						1.9E+02	2.7E+01	1.7E+03	1.7E+02
2.4E+01	6.3E+00						5.6E+01	1.6E+01	7.9E+02	1.7E+02
4.2E+01	5.8E+00						7.4E+01	1.4E+01	5.2E+02	7.0E+01
1.3E+00	3.7E-01						2.7E+01	5.7E+00	1.3E+02	3.3E+01
1.1E-05	1.5E-06	8.5E-01	6.5E-01							
2.3E-05	9.7E-06									
7.1E-05	9.0E-06									
1.4E-04	2.4E-05	1.3E+00	3.1E-01	5.6E-01	1.3E-01	*1.1E+00*				
		3.2E-01	1.6E-01	2.9E-01	1.5E-01	*1.3E+00*				
		1.8E+00	5.4E-01			*1.1E+00*				
1.5E-04	1.1E-04	5.5E-01	3.6E-01	1.1E+00	8.3E-01	*1.5E+00*				
		2.3E+00	1.8E+00			*5.4E-02*				
7.2E-06	5.1E-06	9.7E-01	3.5E-01	2.7E-01	1.1E-01					
7.1E-06	1.0E-06	2.0E-02	1.5E-02	3.7E-02	2.0E-01	*8.9E-02*				
5.6E-05	9.3E-06	5.5E-01	3.4E-01			*1.6E+00*				
1.2E-04	2.9E-05			3.3E-01	2.0E-01	*4.1E-02*				
1.7E-04	1.3E-04	2.6E+00	1.4E+00	1.3E-01	4.9E-02	*5.1E+00*				
8.7E-04	6.7E-04	4.5E-01	8.4E-02	1.4E+00	3.2E-01					
1.1E-05	7.9E-06									
8.0E-04	3.5E-05									
3.8E-02	1.9E-03					*6.2E-02*				
		1.0E+00	8.9E-01			*6.1E+00*				

only one experiment, that olivine-melt D value is consistent with previous studies (Table 7).

Partitioning of Ga

Plagioclase-melt D values for Ga range from 0.76 to 1.2, while pyroxene-melt D values range from 0.12 to 2.2 and olivine-melt D values range from 0.005 to 0.83. Plagioclase-melt, pyroxene-melt, and olivine-melt D values for Ga do not correlate with oxygen fugacity, pressure, or An content of plagioclase. By contrast, there appears to be a weak positive correlation between plagioclase-melt D values and SiO_2 content of the melt (Fig. 4d).

Plagioclase-melt D values for Ga are within the range of results reported by prior studies (Paster et al. 1974; Blundy et al. 1998). The pyroxene-melt D values for Ga range from incompatible to slightly compatible in our charges. Most prior experimental determinations of Ga pyroxene-melt D values reported incompatible behavior (e.g., Adam and Green 2006). Gallium is also incompatible in olivine, however, some of our olivine-melt D values are up to seven times higher than those previously reported by Adam and Green (2006). This may be due to the different compositional and experimental conditions. Adam and Green (2006) used a basanitic composition, with high water contents (≥7.5 wt%), and at generally higher pressures than our runs.

Partitioning of Mo and W

The MSE Mo and W are generally incompatible in all silicate phases examined. The plagioclase-melt D values for Mo range from 1×10^{-4} to 8×10^{-4}. Molybdenum tends to be less incompatible in pyroxene than plagioclase and olivine, with pyroxene-melt D values ranging from 5×10^{-4} to 0.09. Olivine-melt D values for Mo range from 0.0001 to 0.036. The mineral-melt D values for W range from 7×10^{-6} to 1×10^{-4} for plagioclase, 7×10^{-6} to 8×10^{-4} for pyroxene, and 1×10^{-5} to 0.04 for olivine. Mineral-melt D values for Mo and W display no correlations with SiO_2 content of the melt, or An content of plagioclase.

The plagioclase-melt D values for Mo and W we determined are significantly lower than previously

Table 7. Ranges for literature *D* values.

D values	Hf	Sr	Ga	W	Mo	Ru	Pd	Au	Ni	Co
Metal/silicate				0.03–5160	80-4.6E+5	2.4E+6-2E+12	3800-1.6E+7	3300-2.5E+7	28–9560	14–2550
Plagioclase/melt	0.01–0.153	1.18–3.34	0.36–1.7	0.1	0.39	<0.3	<0.2			
Pyroxene/melt	0.15–1.9	0.0012–0.128	0.34–0.77	0.00014–0.05	0.0039–0.012	1.0–4.3				
Olivine/melt	0.0008–0.004	1.5E-5-0.00025	0.005–0.012	0.0001–0.0003	0.0007–0.001	0.67–2.19	0.0061–0.021	0.7		

Metal/silicate data from: Jones and Drake (1986), Hillgren (1993), Borisov et al. (1994), Borisov and Palme (1995), Borisov and Nactweyh (1998), Righter and Drake (1999), Holzheid and Palme (2007), Kegler et al. (2008), Siebert et al. (2011), Tuff et al. (2011), Mann et al. (2012), Wade et al. (2012).

Mineral/melt data from: Paster et al. (1974), Drake and Weill (1975), Luhr et al. (1984), Kloeck and Palme (1988), Capobianco et al. (1991), Hart and Dunn (1993), Beattie (1993, 1994), Dunn and Sen (1994), Blundy et al. (1998), Bindeman and Davis (2000), Hill et al. (2000), Brenan et al. (2003), Bennett et al. (2004), Adam and Green (2006), Klemme et al. (2006), Aigner-Torres et al. (2007).

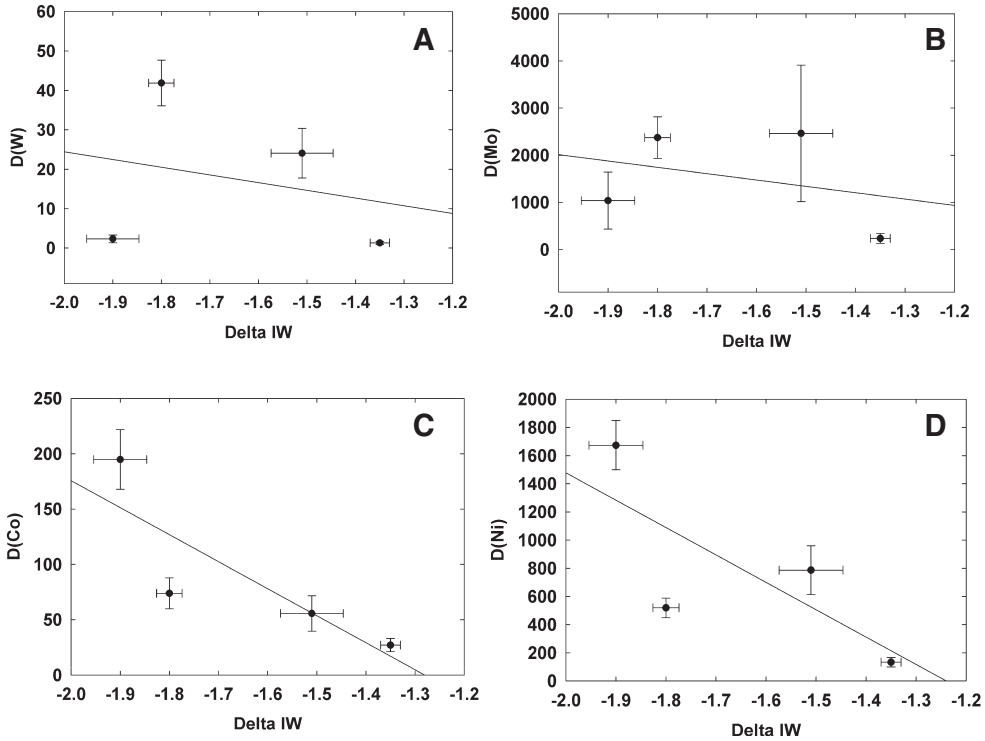

Fig. 3. This figure shows the ΔIW value versus D for W (panel A), Mo (panel B), Co (panel C), and Ni (panel D). We see general decreasing values for D with increasing oxygen fugacity for all elements.

measured values (Luhr et al. 1984; Dunn and Sen 1994) (see Tables 6 and 7). The differences may be due to the different run compositions examined. The *D* value for Mo from Dunn and Sen (1994) was obtained from an experimental series on a calc-alkaline suite of rocks. The *D* value reported for W by Luhr et al. (1984) was an upper limit determined for trachyandesite. Additionally, phenocryst-matrix *D* value determination may overestimate *D* values, due to incorporation of mineral or melt inclusions in the analyses (Bédard 2006). By contrast, pyroxene-melt and olivine-melt *D* values for Mo and W are broadly consistent with previous values (Adam and Green 2006).

Partitioning of Ru, Pd, and Au

Although the HSE were generally below detection limits in both minerals and glass, a few of the mineral and glass analyses were above the detection limit. For the experiments in which mineral and melt compositions could be determined, Ru *D* values for plagioclase-melt and pyroxene-melt varied between 0.32 and 2.3, and 0.02 and 2.6, respectively. The plagioclase-melt *D* values for Ru do not appear to be correlated with SiO_2 content of the melt, or plagioclase An content. Some of our Ru pyroxene-melt *D* values are within the range of Hill et al. (2000), but a few experiments yielded values lower than that study (Tables 5 and 6). The one viable olivine-melt *D* value obtained was 1.0, and is well within the range of values reported by previous studies (Brenan et al. 2003; Righter et al. 2004; Malavergne et al. 2006, 2012). When plotted against oxygen fugacity, however, our new datum does not plot within uncertainty along the trend of decreasing olivine-melt *D* value with increasing fO_2 defined by the prior measurements (Fig. 5). This may be due to the higher pressure of our experiment, performed at 0.7 GPa, compared to the 0.0001 GPa conditions of Brenan et al. (2003) and Righter et al. (2004), or because their experiments do not extend to the lower fO_2 used in our experiment. It may also indicate that a change in Ru valence state occurs over this range of fO_2 that could account for the stabilization of the partition coefficient below log fO_2 −5.

Plagioclase-melt *D* values for Pd range from 0.2 to 1, and the pyroxene-melt *D* values range from 0.04 to 1.3. Only nine glasses and no minerals had measurable concentrations of Au. For these experiments, only upper limits of the partition coefficient could be estimated. This was achieved by dividing the detection limit of the mineral analysis by the concentration determined for the glass. For plagioclase-melt, upper limits for *D* values range from 0.05 to 1.5, for pyroxene-melt *D* value upper limits range from 0.04 to 8.4. Upper limits ranging from 0.06 to 6.1 were obtained for olivine-melt. Our

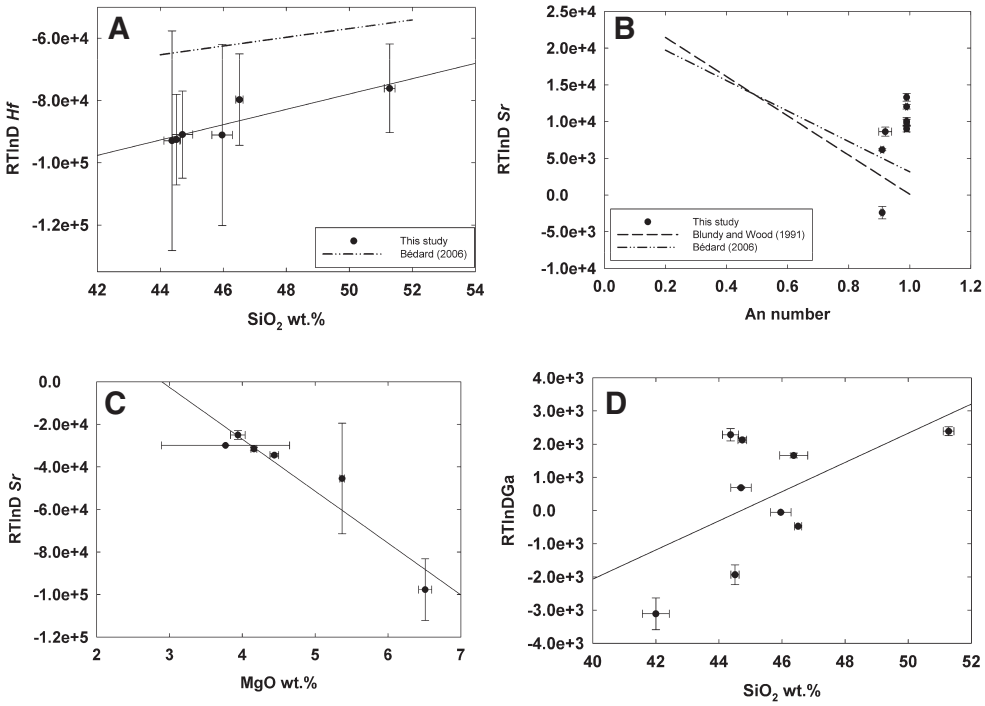

Fig. 4. Panel A shows SiO_2 wt% of the melt versus RTlnD for Hf in plagioclase. There is a clear trend of increasing plagioclase-melt D with increasing SiO_2 wt% in Hf, except for one outlier. The trend in Hf is offset from the Bédard (2006) study. Panel B shows An number versus RTlnD for Sr. We have plotted the Bédard (2006) and Blundy and Wood (1991) regressions where available. Our Sr plagioclase-melt *D* values are not matched well by either of the regressions. This figure also shows trend a trend in pyroxene in panel C. The first plot shows MgO wt% of the melt versus RTlnD for Sr in pyroxene. Panel D shows SiO_2 wt% of the melt versus RTlnD for Ga in plagioclase, where there is a potential positive correlation.

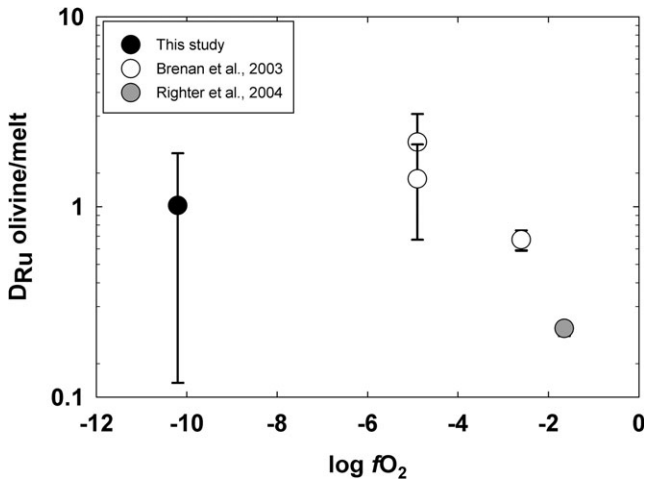

Fig. 5. This figure plots log fO_2 versus D of Ru in olivine. We also plot data from Brenan et al. (2003) and Righter et al. (2004). Our sample indicates that the increasing olivine-melt D with decreasing oxygen fugacity does not extend to much lower log fO_2 values.

experiments confirm that both Pd and Au are generally incompatible in plagioclase, consistent with previous studies (Capobianco et al. 1991). Pyroxene-melt *D* values for Pd and Au indicate that these elements can be compatible or incompatible depending on conditions. The upper limit of 6.1 for the olivine-melt *D* value for Au is much higher than the value of 0.7 reported by Kloeck and Palme (1988). Given that our *D* value is a maximum, it may be within the range of Kloeck and Palme (1988). No olivine-melt *D* values for Pd could be determined from our experiments.

DISCUSSION

A major objective of this study is to better constrain abundances of certain siderophile and lithophile elements in the lunar mantle, especially during evolution of the putative LMO. We do this via two independent approaches. First, we combine two compositional models for the Moon with metal-silicate distribution coefficients derived from a trace element partitioning parameterization. The parameterization is strengthened for conditions appropriate to conditions of lunar core segregation by incorporation of our new experimental results. From this we estimate elemental abundances in the bulk silicate Moon immediately following core segregation. Second, constraints on abundances of the elements in the LMO at the time of plagioclase flotation are made using simple crystal-

liquid fractionation models. This approach combines the observed abundances of various siderophile and lithophile trace elements in the Moon's anorthositic crust, with newly determined mineral-silicate distribution coefficients. Through reverse modeling, we calculate abundances of the trace elements in the LMO at the time of plagioclase flotation.

Initial Establishment of Siderophile Elements in the LMO via Core Segregation

The siderophile trace element compositions of the terrestrial and lunar mantles were likely initially established by core formation. Numerous prior studies (e.g., Jana and Walker 1997; Righter and Drake 1999; Holzheid et al. 2000; Mann et al. 2012) have investigated metal-silicate partitioning of siderophile elements as functions of pressure, temperature, and composition. For example, at low pressures, the HSE are defined as having metal-silicate partition coefficients greater than 10^4 (e.g., O'Neill et al. 1995; Walter et al. 2000). By contrast, high pressures and temperatures tend to lower D values for at least some siderophile elements. Righter et al. (2008) found that at higher pressures (approximately 10–15 GPa), metal-silicate partition coefficients for Pd decrease enough to account for terrestrial mantle abundances of HSE. There is some inconsistency in the literature, however, with respect to generalizations. For example, Holzheid et al. (2000) conversely reported that the metal-silicate D values for Pd do not vary with pressure. The discrepancy between the two studies has been attributed to differences in the experimental compositions used by each study (Righter et al. 2008). Consequently, when considering lunar differentiation, it is especially important to determine metal-silicate partitioning for P–T–x conditions most relevant to lunar core formation.

One approach to determining relevant D values for LMO conditions is through parameterization of partitioning data obtained over wide-ranging conditions. Effects of fO_2, T, P, and melt composition have been previously parameterized for metal-silicate D values for some siderophile elements by Righter et al. (2010) and Righter (2011). Their parameterizations are as follow:

$$\ln D = a\ln(fO_2) + \frac{b}{T} + \frac{cP}{T} + d\left(\frac{\text{nbo}}{t}\right) + e\ln(1 - X_S) + f\ln(1 - X_C) + g \quad (2)$$

$$\ln D = a\ln(fO_2) + \frac{b}{T} + \frac{cP}{T} + \sum d_i X_i + e\ln(1 - X_S) + f\ln(1 - X_C) + g \quad (3)$$

In both equations, the values for parameters a–g were determined by regressions of literature partitioning data for the element of interest. The fO_2 term represents the absolute oxygen fugacity, which is calculated using Equation 1 and the IW buffer expression of Righter et al. (1997), unless reported in the original paper. In these equations, P and T represent pressure and temperature, respectively. The elements sulfur and carbon are known to have significant effects on metal-silicate partitioning of siderophile elements, so their abundances are represented in the parameterizations as X_S and X_C, the mole fractions of sulfur and carbon, respectively. Equation 2 is used to model D values for Ni, Co, Ru, Pd, and Au. In Equation 2, the number of nonbridging oxygen atoms per tetrahedral cation (nbo/t) represents the degree of polymerization in the melt (Mysen 1991). Equation 3 is used to model D values for Mo and W because they are more sensitive to melt composition than Ni and Co, which are well modeled by the nbo/t parameter. In Equation 3, the nbo/t parameter has been replaced by the summation of a series of oxide mole fractions (including Si, Al, Ca, Mg, and Fe) that more accurately reflect the melt composition effects on the metal-silicate D values for Mo and W (Righter et al. 2010).

The literature data used in the regressions include all available data for Mo, W, Ni, and Co at pressures <5 GPa, the central pressure of the Moon. Our new experimental data are more relevant to lunar core-segregation conditions (P, T, fO_2, and melt composition). Consequently, incorporating them into the larger data set strengthens the parameterization in the P–T–X region most similar to LMO conditions. Plots of measured D values compared to the calculated D values are presented for both literature values and our metal-silicate experiments (Fig. 6). Our new metal-silicate experiments overlap with the literature data set for all elements examined. For Au, Pd, and Ru, all available data, even those conducted at pressures >5 GPa, are included in the regression. This is necessary because of the limited availability of partitioning data for these three elements (see Righter et al. 2014). Once the parameters a–g are defined by the literature regression, we can change the input for P, T, fO_2, and melt composition to explore various conditions for lunar core formation. The revised regression parameters for Equations 2 and 3 are listed in Table 8.

To estimate the metal-silicate D values for Mo, W, Co, Ni, Ru, Pd, and Au at the time of core formation, we used the following parameters: oxygen fugacity of IW-1.25, pressure of 4.5 GPa, and temperature of 1800 °C. We applied the silicate-melt compositions and nbo/t from Longhi (2006). In this model we used constant X_S and X_C values of 0.08 and 0.02, respectively

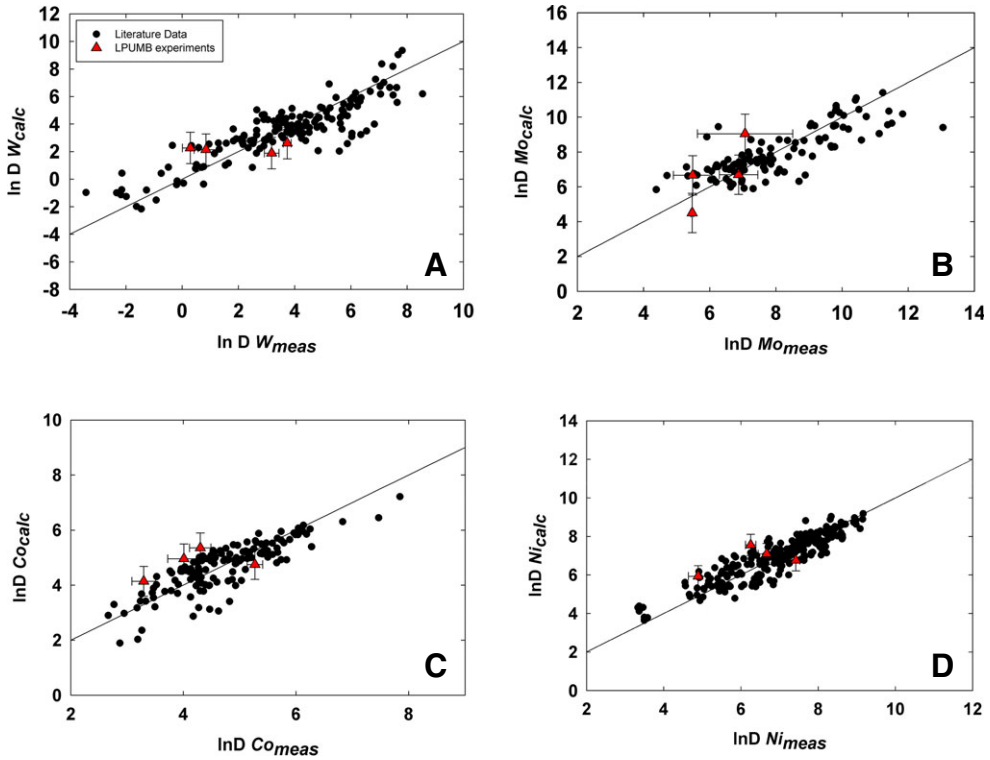

Fig. 6. This figure shows $\ln D_{meas}$ versus $\ln D_{calc}$. for W (panel A), Mo (panel B), Co (panel C), and Ni (panel D). The metal-silicate D values for W are well modeled by the regression calculation. Also plotted is the 1:1 line. Literature data come from Newsom and Drake (1982); Seifert et al. (1988); Hillgren (1993); Peach and Mathez (1993); Thibault and Walter (1995); Holzheid and Palme (1996); Walter and Thibault (1995); Li and Agee (1996); Hillgren et al. (1996); Gaetani and Grove (1997); Jana and Walker (1997); Righter et al. (1997); Righter and Drake (1999); Li and Agee (2001); Bouhifd and Jephcoat (2003); Wade and Wood (2005); Corgne et al. (2008); Holzheid and Palme (2007); Kegler et al. (2008); Cottrell et al. (2009); Righter et al. (2010); Siebert et al. (2011); Tuff et al. (2011); Wade et al. (2012); Righter et al. (2013).

(Garcia et al. 2011). The S and C contents are consistent with previous geochemical studies (siderophile element partitioning and S and C contents of melt inclusions in olivines; Righter 2002; Rai and Van Westrenen 2014; Wetzel et al. 2013), as well as thermal modeling (Laneuville et al. 2013; Zhang et al. 2013).

Using D values obtained from parameterization, we estimated the concentrations of Mo, W, Ni, Co, Ru, Pd, and Au in the silicate portion of the lunar magma ocean during the conditions of core formation, following the method of Hillgren (1991), by applying the following mass balance equation:

$$C^i_{sil} = \frac{C^i_{bulk}}{\left[x + (1-x)\left(D^i_{\frac{met}{sil}}\right)\right]} \quad (4)$$

For this equation, C^i_{sil} is the concentration of trace element i in the silicate portion of the Moon, i.e., the bulk silicate Moon. It is the unknown in our calculations. Additionally, x represents the fraction of core (by mass). Here, we use 0.984, based on the assumption that the metallic core of the Moon comprises a fraction of 0.016 (Garcia et al. 2011). The C^i_{bulk} term is the concentration of the same element in the bulk Moon. As previous models for bulk lunar compositions were generated using data from lunar basalts and make assumptions about the size of the core and metal-silicate D values (e.g., O'Neill 1991), here we estimate bulk compositions for the Moon based on two formational models that are independent of basalt compositions (Table 9). In the first model, we assume the siderophile element content of the bulk Moon is equivalent to the composition of the terrestrial primitive mantle (PM). Siderophile element concentrations used come from Palme and O'Neill (2003), Becker et al. (2006), and Fischer-Gödde et al. (2011). This model is valid if the Moon formed entirely from silicates derived from the mantle of the giant impactor and terrestrial mantle, assuming the siderophile element abundances in these mantles had been established at PM levels by core segregation and/or accretionary processes prior to the impact. It also assumes the lunar core formed by reduction in Fe during lunar coalescence. One caveat to

Table 8. Constants derived from linear regressions.

	a (fO_2)	$b(1/T)$	c (P/T)	d (nbo/t)	d XSi	d XAl	d XFe	d XMg	d XCa	e (ln(1–X_S))	f (ln(1–X_C))	g	n	Std. error
Ni	−0.454	−20,477	287	−0.38						−2.39	−1.1	9.11	249	0.54
Co	−0.391	−20,668	355	−0.27						−0.99	−0.85	8	152	0.50
W	−0.61	−45,660	1950		14.54	3.9	−21.96	−5.8	4.53	7.87	−9.17	11.3	167	1.14
Mo	−0.22	−17,420	186		0.51	1.39	−14.73	−9.28	−8.71	−0.97	−1.83	16.97	114	1.09
Ru	−0.14	−20,550	2.1	−2.6						9.4	32.1	28	32	1.14
Pd	−0.16	11,800	6.8	−1.47						7.1	15.1	5.57	135	0.82
Au	−0.155	15,650	31.4	−0.23						9	3.8	−0.23	85	0.95

n is the number of analyses used to determine the regression.

this formational model is that terrestrial PM composition may contain a late accretionary signature that could largely postdate lunar differentiation. The siderophile element composition of the Moon, as defined by primary accretion and differentiation of either the impactor or the pre-giant impact Earth are unknown, thus, we use the terrestrial PM as a reasonable estimate of the silicate composition.

For the second model we use 98.4% PM plus 1.6% terrestrial core composition (McDonough 2003) as an upper limit for the trace element concentrations. This model assumes that a small fraction of core material of either the Earth or the giant impactor was incorporated into the forming Moon. This core material would make up the entirety of the current lunar core and have element abundances equivalent to the terrestrial core.

In Fig. 7a, we plot the CI chondrite normalized abundances of literature estimates for the lunar mantle (from Palme et al. 1984; O'Neill 1991; Walter et al. 2000; Ranen and Jacobsen 2004; Day et al. 2007) in comparison to our model results derived generated using the new metal-silicate partition coefficients. We also plot abundances for the terrestrial PM, the terrestrial core, and the mixture of the two used in the second bulk compositional model. The core-segregation model using a PM bulk composition for the Moon yields trace element abundances that are generally lower than the prior lunar mantle estimates. The results of the core-segregation model with a bulk composition of PM with a small fraction of terrestrial core overlap with lunar mantle estimates from the literature for all elements, except for Ru (Palme et al. 1984; O'Neill 1991; Walter et al. 2000; Ranen and Jacobsen 2004; Day et al. 2007) (Fig. 7a). This is also consistent with lunar formation hydrodynamic simulations (e.g., Ćuk and Stewart 2012), which derive the lunar core from the cores of the impactor and the proto-Earth. Note, however, that estimates for the abundances of these siderophile trace elements in the lunar mantle were generally projected from basalts by using correlations between elements of equivalent compatibility. The lunar mantle estimates may not be representative of the whole lunar mantle due to potential heterogeneity in source regions.

Constraining concentrations of siderophile elements following core-mantle differentiation does not alone provide new insights to address evolution of the LMO or potential incorporation of additional meteoritic material postcore formation. After core formation, crystallization of the various minerals precipitating from the LMO would have led to fractionation of siderophile and lithophile trace elements. Most estimates place the arrival of plagioclase on the liquidus of the LMO following about 75% crystallization (e.g., Snyder et al. 1992). Thus, abundances of highly incompatible trace elements may have been enriched, relative to the initial bulk silicate Moon, by factors of 4–20 due concentration in the residual liquid during fractional crystallization.

Estimation of Trace Element Abundances in the LMO at the Time of Plagioclase Crystallization

As lunar ferroan anorthosites have been proposed to be a crystallization product of the LMO, the compositions of these rocks are used to model the LMO composition at the time of plagioclase crystallization utilizing the new plagioclase-melt D values (Table 9). The concentrations of the elements in the LMO at time of plagioclase flotation are calculated by taking average concentrations of the elements observed in lunar anorthosites and dividing by the respective plagioclase-melt D value. Lunar anorthosite data from Wänke et al. (1975) (W), Norman et al. (2003) (Sr, Hf, Mo, Ni, Co), and Day et al. (2010) (Ru, Pd, and Au) are used in the calculations. We use the highest and lowest D values obtained to establish the range for possible LMO concentrations. The model results in concentrations of 3–21 ppt for Ru, 30–120 ppt for Pd, 2.5–4.1 ppm for Ga, 25–190 ppm for Mo, 100–2100 ppm for W, 50–190 ppm for Sr, and 700–4400 ppm for Hf. The plagioclase-melt D values for Au are estimated from the limit of detection of Au in the mineral and the measured concentration in the

Table 9. Concentration estimates for lunar bulk composition and lunar mantle.

	Ru (ppb)	Pd (ppb)	Au (ppb)	Mo (ppm)	Ga (ppm)	W (ppm)	Sr (ppm)	Hf (ppm)	Ni (ppm)	Co (ppm)
Bulk moon estimates										
PM	7.2	7.1	1.7	0.039	4.4	0.016	20.3	0.3	1860	102
98.4%PM+1.6% Terrestrial core	71	57	10	0.118		0.023			2662	140
Anorthosite	0.007	0.033	0.028	0.02	3.1	0.015	156	0.26	49	16
Core-segregation model-PM	0.002	0.051	0.023	0.001		0.005			189	44
Core-segregation model-PM+TC	0.024	0.402	0.13	0.004		0.007			271	61
Low plagioclase-melt estimate	0.003	0.03	0.02	26	2.5	100	51	696	42	10
High plagioclase-melt estimate	0.02	0.12	0.52	190	4.1	2095	192	4409	400	180
Lunar mantle literature	0.10	0.10	0.12–1.2	0.0022	0.66–2.8	0.0056–0.018	13–80	0.17	470	90
Orgueil	686	558	146	0.973	9.71	0.096	7.81	0.106	10,800	580
CI normalized										
PM	1.05E-02	1.27E-02	1.16E-02	4.01E-02	4.53E-01	1.67E-01	2.60E+00	2.83E+00	1.72E-01	1.76E-01
98.4%PM+1.6% Terrestrial core	1.03E-01	1.02E-01	6.85E-02	1.21E-01		2.40E-01			2.47E-01	2.41E-01
Core-segregation model-PM	2.9E-06	9.1E-05	1.6E-04	1.0E-03		5.2E-02			1.8E-02	7.6E-02
Core-segregation model-PM+TC	3.5E-05	7.2E-04	8.9E-04	4.1E-03		7.3E-02			2.5E-02	1.1E-01
Low plagioclase-melt estimate	4.4E-06	5.4E-05	1.3E-04	2.7E+01	2.6E-01	1.0E+03	6.5E+00	6.6E+03	3.9E-03	1.7E-02
High plagioclase-melt estimate	3.1E-05	2.2E-04	3.6E-03	2.0E+02	4.2E-01	2.2E+04	2.5E+01	4.2E+04	3.7E-02	3.1E-01
Lunar mantle literature	1.5E-04	1.8E-04	8.2E-04-8.2E-03	2.3E-03	6.8E-02-2.9E-01	5.8E-02-1.9E-01	1.6E+00-1.0E+01	1.6E+00	4.4E-02	1.6E-01

Orgueil values used in CI normalization come from Lodders (2010). Anorthosite values from Wänke et al. (1975) for W; Norman et al. (2003) for Sr, Ga, Hf, Mo, Co, Ni; Day et al. (2007) for Ru, Pd, and Au. Plagioclase-melt estimates for Ni and Co are calculated from *D* values in Bindeman et al. (1998). Lunar mantle literature concentrations from: Palme et al. (1984) for Ga, Sr; O'Neill (1991) for Mo, Ga, W, Ni, Co; Walter et al. (2000) for Au; Ranen and Jacobsen (2004) for W, Sr; Hf, Day et al. (2007) for Ru, Pd, Au. Terrestrial core concentrations from McDonough (2003).

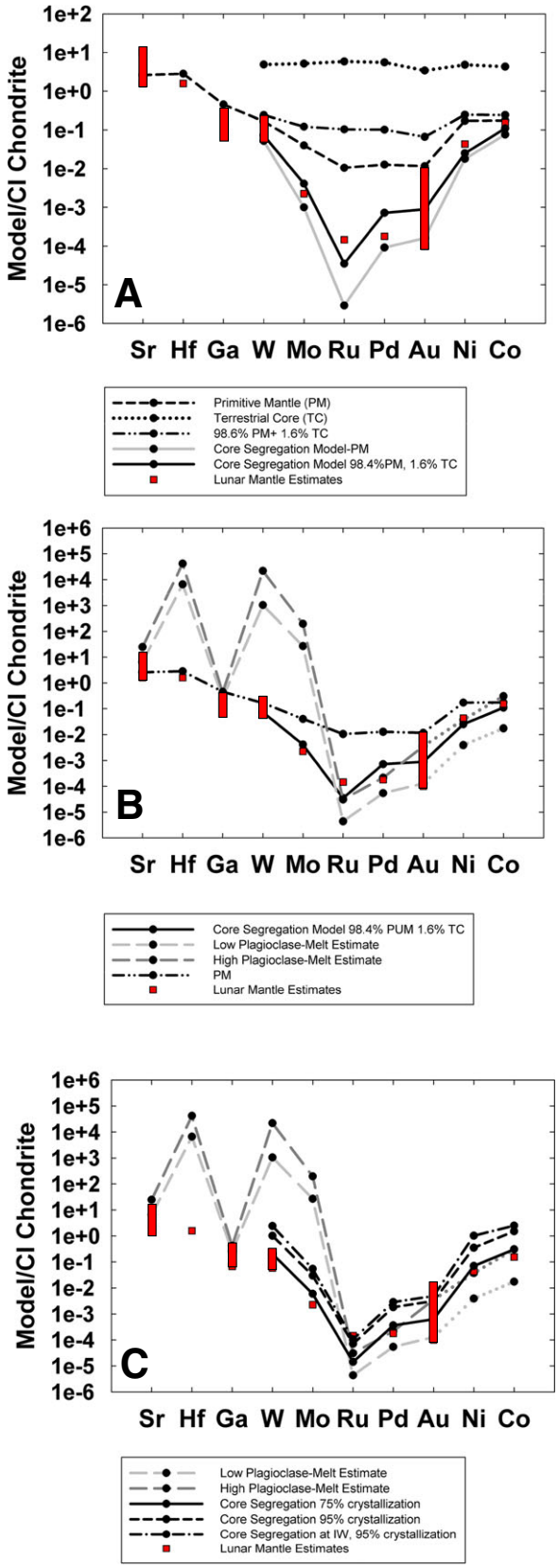

Fig. 7. Panel A is a chondrite normalized (Orgueil) plot of the calculated estimates from regressions for two bulk compositions at conditions of core formation for trace elements Sr, Hf, Ga, W, Mo, Ru, Pd, and Au. In addition to the core-segregation model, we plot the starting materials of PM (Palme and O'Neill 2003; Becker et al. 2006; and Fischer-Gödde et al. 2011), terrestrial core (McDonough 2003), and PM plus terrestrial core. Panel B shows the upper and lower estimates from plagioclase-melt *D* values for the LMO at time of plagioclase crystallization. The second bulk composition result for the core-segregation model is also plotted. Panel C shows the upper and lower estimates from the plagioclase-melt *D* values and the core-segregation models at two different times: at 75% crystallization and 95% crystallization. At 95% crystallization, we test changes in oxygen fugacity. Also plotted on all panels are lunar mantle estimates from literature (Palme et al. 1984; O'Neill 1991; Walter et al. 2000; Ranen and Jacobsen 2004; Day et al. 2007). The dotted lines in the plagioclase-melt estimates indicates that the *D* values used in this calculation were not determined by this study, but were taken from Bindeman et al. (1998).

corresponding glass. This gives the maximum *D* value, so the calculated range of 18–518 ppt for Au is a lower limit. We can also use previously determined plagioclase-melt *D* value ranges from Bindeman et al. (1998) to estimate concentrations of Ni and Co in the LMO. The range of concentrations for Ni is 40–400 ppm and the range for Co is 10–180 ppm.

When plotted in Fig. 7b, the new LMO estimates are compared to previous lunar mantle estimates, as well as the core-segregation model. In comparison to lunar mantle estimates, calculated Sr, Ga, Pd, and Au abundances are within range; Hf, W, and Mo are higher; and Ru is lower. In comparison to PM from Palme and O'Neill (2003): Ga, Ru, Pd, and Au are depleted and Sr, Hf, W, and Mo are enriched. The depletions of Ru and Pd of more than a factor of 20 with respect to PM are consistent with the results of Walker et al. (2004) and Day et al. (2007). When the core-segregation model is compared to the plagioclase-melt *D* value model, the concentrations of Ru, Pd, and Au are similar to within an order of magnitude, indicating that during the time between core segregation and plagioclase formation, the HSE concentration of the LMO was not significantly changed, consistent with their mildly incompatible nature (bulk *D* approximately 1). The LMO abundances of Mo and W are much higher than those determined for the bulk silicate Moon obtained from the core-segregation model. If the core-segregation model sets the initial siderophile element signature of the LMO, this suggests that Mo and W were further concentrated in the remaining melt during the crystallization of the LMO. We explore several possible explanations for these enrichments, including

incompatibility during fractional crystallization, core segregation at higher fO_2 than IW-1.25, high doping levels in the experiments, and use of bulk anorthosite data rather than plagioclase separate data.

The high concentrations of Hf, W, and Mo predicted by the plagioclase-D value model may be the consequence of enrichment, as compared to the original melt concentration, due to the extreme incompatibility of these elements in a small melt fraction at the time of plagioclase crystallization. In Fig. 7c, we show the effect of fractional crystallization on the PM and 1.6% terrestrial core bulk compositional model at 25% melt fraction, the level of enrichment produced by fractional crystallization would only be about a factor 4, assuming complete incompatibility, which is not enough to explain Hf, W, and Mo concentrations. It is possible that the anorthosites formed later in the crystallization process, but even when the melt fraction is reduced to 5%, the corresponding increase in the enrichment is still only about a factor of 20, which is not enough to explain the enrichments.

The core-segregation model itself is sensitive to changes in pressure, temperature, composition, and oxygen fugacity. Thus, in addition to melt fraction, we show the effect of raising the oxygen fugacity on the core-segregation model with a 5% melt fraction in Fig. 7c. The results are still not high enough to account for the enrichment in W and Mo. We made additional changes in pressure and temperature, but they did not significantly change the concentrations predicted by the model, so are not shown. Another potential issue is that the high concentration estimates for Hf, W, and Mo may be due to underestimation of D values that stem from extremely high concentrations in the glass that may be related to the addition of trace elements at wt% levels.

Alternatively, the high concentrations predicted for Hf, W, and Mo may be related to the anorthosite concentrations that we are using in the calculation. In bulk anorthosite, there could be trace amounts of minor phases such as ilmenite, pyroxene, or spinel that could contribute to the bulk inventory of Hf, W, and Mo (e.g., Klemme et al. 2006; Righter and Shearer 2003). Comparing Hf concentrations in both Norman et al. (2003) of a bulk anorthosite clast (0.26 ppm) to plagioclase separates (0.008 ppm) in Touboul et al. (2009), it is apparent that this effect could account for much of the extreme enrichment.

CONCLUSIONS

Our new D values for both metal-silicate and mineral-melt partitioning experiments are generally consistent with those reported in previous studies. The metal-silicate regression derived lunar mantle estimate is consistent with previous lunar mantle estimates, consistent with the interpretation that lunar core formation occurred in a deep magma ocean. Mineral-melt derived LMO compositions for Ru, Pd, and Au are similar to the values derived from core-segregation models, consistent with these elements being mildly incompatible to compatible during magma ocean crystallization. The mineral-melt derived LMO compositions are characterized by enrichments in Hf, W, and Mo. These enrichments of Hf, W, and Mo are much greater than would be predicted by fractional crystallization of the LMO; some of the latter enrichment may be influenced by the use of bulk anorthosite data rather than plagioclase separates.

Acknowledgments—We gratefully acknowledge the experimental support provided by Lisa Danielson and Kellye Pando. We also thank Philip Piccoli for assistance with EPMA data collection at the Nanoscale Imaging, Spectroscopy, and Properties Laboratory and Richard Ash for assistance with collection of laser ablation data. This research was partially supported by NASA NLSI grant NNA09DB33A (to R. J. Walker), and RTOPs from the NASA LASER and NLSI programs (to K. Righter). M. Sharp was supported by the NASA Harriett G. Jenkins Pre-doctoral Fellowship NNX10AU20A. We also acknowledge the great feedback from our reviewers (James Brenan and one anonymous reviewer) and associate editor Nancy Chabot.

Editorial Handling—Dr. Nancy Chabot

REFERENCES

Adam J. and Green T. 2006. Trace element partitioning between mica and amphibole-bearing garnet lherzolite and hydrous basanitic melt: 1. Experimental results and the investigation of controls on partitioning behaviour. *Contributions to Mineralogy and Petrology* 152:1–17.

Aigner-Torres M., Blundy J., Ulmer P., and Pettke T. 2007. Laser ablation ICPMS study of trace element partitioning between plagioclase and basaltic melts: An experimental approach. *Contributions to Mineralogy and Petrology* 153:647–667.

Beattie P. 1993. Olivine-melt and orthopyroxene-melt equilibria. *Contributions to Mineralogy and Petrology* 115:103–111.

Beattie P. 1994. Systematics and energetics of trace-element partitioning between olivine and silicate melts: Implications for the nature of mineral/melt partitioning. *Chemical Geology* 117:57–71.

Becker H., Horan M. F., Walker R. J., Gao S., Lorand J. P., and Rudnick R. L. 2006. Highly siderophile element composition of the Earth's primitive upper mantle: Constraints from new data on peridotite massifs and xenoliths. *Geochimica et Cosmochimica Acta* 70:4528–4550.

Bédard J. H. 2006. Trace element partitioning in plagioclase feldspar. *Geochimica et Cosmochimica Acta* 70:3717–3742.

Bennett S., Blundy J., and Elliott J. 2004. The effect of sodium and titanium on crystal-melt partitioning of trace elements. *Geochimica et Cosmochimica Acta* 68:2335–2347.

Bindeman I. N. and Davis A. M. 2000. Trace element partitioning between plagioclase and melt: Investigation of dopant influence on partition behavior. *Geochimica et Cosmochimica Acta* 64:2863–2878.

Bindeman I. N., Davis A. M., and Drake M. J. 1998. Ion microprobe study of plagioclase-basalt partition experiments at natural concentration levels of trace elements. *Geochimica et Cosmochimica Acta* 62:1175–1193.

Blundy J. D. and Wood B. J. 1991. Crystal-chemical controls on the partitioning of Sr and Ba between plagioclase feldspar, silicate melts, and hydrothermal solutions. *Geochimica et Cosmochimica Acta* 55:193–209.

Blundy J. D., Robinson J. A. C., and Wood B. J. 1998. Heavy REE are compatible in clinopyroxene on the spinel lherzolite solidus. *Earth and Planetary Science Letters* 160:493–504.

Borisov A. and Nactweyh K. 1998. Ru solubility in silicate melts: experimental results in oxidizing region (abstract #1320). 29th Lunar and Planetary Science Conference. p. 1320.

Borisov A. and Palme H. 1995. The solubility of iridium in silicate melts: New data from experiments with $Ir_{10}Pt_{90}$ alloys. *Geochimica et Cosmochimica Acta* 59:481–485.

Borisov A. and Palme H. 1996. Experimental determination of the solubility of Au in silicate melts. *Mineralogy and Petrology* 56:297–312.

Borisov A., Palme H., and Spettel B. 1994. Solubility of palladium in silicate melts: Implications for core formation in the Earth. *Geochimica et Cosmochimica Acta* 58:705–716.

Bottke W. F., Walker R. J., Day J. M., Nesvorny D., and Elkins-Tanton L. 2010. Stochastic late accretion to Earth, the Moon, and Mars. *Science* 330:1527–1530.

Bouhifd M. A. and Jephcoat A. P. 2003. The effect of pressure on partitioning of Ni and Co between silicate and iron-rich metal liquids: A diamond-anvil cell study. *Earth and Planetary Science Letters* 209:245–255.

Brenan J. M. and McDonough W. F. 2009. Core formation and metal–silicate fractionation of osmium and iridium from gold. *Nature Geoscience* 2:798–801.

Brenan J. M., McDonough W. F., and Dalpe C. 2003. Experimental constraints on the partitioning of rhenium and some platinum-group elements between olivine and silicate melt. *Earth and Planetary Science Letters* 212:135–150.

Campbell A. J., Humayun M., and Weisberg M. K. 2002. Siderophile element constraints on the formation of metal in the metal-rich chondrites Bencubbin, Weatherford, and Gujba. *Geochimica et Cosmochimica Acta* 66:647–660.

Canup R. M. and Asphaug E. 2001. Origin of the Moon in a giant impact near the end of the Earth's formation. *Nature* 412:708–712.

Capobianco C. J., Drake M. J., and Rogers P. S. Z. 1991. Crystal/melt partitioning of Ru, Rh and Pd for silicate and oxide phases (abstract #1089). 22nd Lunar and Planetary Science Conference. pp. 179–180.

Corgne A., Keshav S., Wood B. J., McDonough W. F., and Fei Y. 2008. Metal–silicate partitioning and constraints on core composition and oxygen fugacity during Earth accretion. *Geochimica et Cosmochimica Acta* 72:574–589.

Cottrell E. and Walker D. 2006. Constraints on core formation from Pt partitioning in mafic silicate liquids at high temperatures. *Geochimica et Cosmochimica Acta* 70:1565–1580.

Cottrell E., Walter M. J., and Walker D. 2009. Metal–silicate partitioning of tungsten at high pressure and temperature: Implications for equilibrium core formation in Earth. *Earth and Planetary Science Letters* 281:275–287.

Ćuk M. and Stewart S. T. 2012. Making the Moon from a fast-spinning Earth: A giant impact followed by resonant despinning. *Science* 338:1047–1052.

Day J. M., Pearson D. G., and Taylor L. A. 2007. Highly siderophile element constraints on accretion and differentiation of the Earth-Moon system. *Science* 315:217–219.

Day J., Walker R. J., James O. B., and Puchtel I. S. 2010. Osmium isotope and highly siderophile element systematics of the lunar crust. *Earth and Planetary Science Letters* 289:595–605.

Dowty E., Prinz M., and Keil K. 1974. Ferroan anorthosite: A widespread and distinctive lunar rock type. *Earth and Planetary Science Letters* 24:15–25.

Drake M. J. and Weill D. F. 1975. Partition of Sr, Ba, Ca, Y, Eu^{2+}, Eu^{3+}, and other REE between plagioclase feldspar and magmatic liquid: An experimental study. *Geochimica et Cosmochimica Acta* 39:689–712.

Dunn T. and Sen C. 1994. Mineral/matrix partition coefficients for orthopyroxene, plagioclase, and olivine in basaltic to andesitic systems: A combined analytical and experimental study. *Geochimica et Cosmochimica Acta* 58:717–733.

Eggins S. M., Kinsley L. P. J., and Shelley J. M. G. 1998. Deposition and element fractionation processes during atmospheric pressure laser sampling for analysis by ICP-MS. *Applied Surface Science* 127:278–286.

Elkins-Tanton L. T., Burgess S., and Yin Q. Z. 2011. The lunar magma ocean: Reconciling the solidification process with lunar petrology and geochronology. *Earth and Planetary Science Letters* 304:326–336.

Ertel W., O'Neill H. S. C., Sylvester P. J., and Dingwell D. B. 1999. Solubilities of Pt and Rh in a haplobasaltic silicate melt at 1300 °C. *Geochimica et Cosmochimica Acta* 63:2439–2449.

Ertel W., Dingwell D. B., and Sylvester P. J. 2008. Siderophile elements in silicate melts—A review of the mechanically assisted equilibration technique and the nanonugget issue. *Chemical Geology* 248:119–139.

Filiberto J., Treiman A. H., and Le L. 2008. Crystallization experiments on a Gusev Adirondack basalt composition. *Meteoritics & Planetary Science* 43:1137–1146.

Fischer-Gödde M., Becker H., and Wombacher F. 2011. Rhodium, gold and other highly siderophile elements in orogenic peridotites and peridotite xenoliths. *Chemical Geology* 280:365–383.

Gaetani G. A. and Grove T. L. 1997. Partitioning of moderately siderophile elements among olivine, silicate melt, and sulfide melt: Constraints on core formation in the Earth and Mars. *Geochimica et Cosmochimica Acta* 61:1829–1846.

Garcia R. F., Gagnepain-Beyneix J., Chevrot S., and Lognonné P. 2011. Very preliminary reference Moon model. *Physics of the Earth and Planetary Interiors* 188:96–113.

Hart S. R. and Dunn T. 1993. Experimental cpx/melt partitioning of 24 trace elements. *Contributions to Mineralogy and Petrology* 113:1–8.

Hartmann W. K. and Davis D. R. 1975. Satellite-sized planetesimals and lunar origin. *Icarus* 24:504–515.

Hill E., Wood B. J., and Blundy J. D. 2000. The effect of Ca-Tschermaks component on trace element partitioning between clinopyroxene and silicate melt. *Lithos* 53:203–215.

Hillgren V. J. 1991. Partitioning behavior of NI, CO, MO, and W between basaltic liquid and Ni-rich metal: Implications for the origin of the moon and lunar core formation. *Geophysical Research Letters* 18:2077–2080.

Hillgren V. J. 1993. Partitioning behavior of moderately siderophile elements in Ni-rich systems: Implications for the Earth and Moon. Ph.D. thesis, University of Arizona, Tucson, Arizona.

Hillgren V. J., Drake M. J., and Rubie D. C. 1996. High pressure and high temperature metal-silicate partitioning of siderophile elements: The importance of silicate liquid composition. *Geochimica et Cosmochimica Acta* 60:2257–2263.

Holzheid A. and Palme H. 1996. The influence of FeO on the solubilities of cobalt and nickel in silicate melts. *Geochimica et Cosmochimica Acta* 60:1181–1193.

Holzheid A. and Palme H. 2007. The formation of eucrites: Constraints from metal-silicate partition coefficients. *Meteoritics & Planetary Science* 42:1817–1829.

Holzheid A., Sylvester P., O'Neill H. S. C., Rubie D. C., and Palme H. 2000. Evidence for a late chondritic veneer in the Earth's mantle from high-pressure partitioning of palladium and platinum. *Nature* 406:396–399.

Jackson S. 2008. LAMTRACE data reduction software for LA-ICP-MS. Laser ablation ICP-MS in the Earth sciences: Current practices and outstanding issues. *Mineralogical Association of Canada, Short Course Series* 40:305–307.

Jana D. and Walker D. 1997. The influence of silicate melt composition on distribution of siderophile elements among metal and silicate liquids. *Earth and Planetary Science Letters* 150:463–472.

Jochum K. P. and Nohl U. 2008. Reference materials in geochemistry and environmental research and the GeoReM database. *Chemical Geology* 253:50–53.

Jones J. H. and Drake M. J. 1986. Geochemical constraints on core formation in the earth. *Nature* 322:221–228.

Kegler P., Holzheid A., Frost D. J., Rubie D. C., Dohmen R., and Palme H. 2008. New Ni and Co metal-silicate partitioning data and their relevance for an early terrestrial magma ocean. *Earth and Planetary Science Letters* 268:28–40.

Klemme S., Günther D., Hametner K., Prowatke S., and Zack T. 2006. The partitioning of trace elements between ilmenite, ulvospinel, armalcolite and silicate melts with implications for the early differentiation of the moon. *Chemical Geology* 234:251–263.

Kloeck W. and Palme H. 1988. Partitioning of siderophile and chalcophile elements between sulfide, olivine, and glass in a naturally reduced basalts from Disko Island, Greenland. Proceedings, 18th Lunar and Planetary Science Conference. pp. 471–483.

Laneuville M., Wieczorek M. A., Breuer D., and Tosi N. 2013. Asymmetric thermal evolution of the Moon. *Journal of Geophysical Research: Planets* 118:1435–1452.

Laurenz V., Fonseca R. O., Ballhaus C., Jochum K. P., Heuser A., and Sylvester P. J. 2013. The solubility of palladium and ruthenium in picritic melts: 2. The effect of sulfur. *Geochimica et Cosmochimica Acta* 108:172–183.

Li J. and Agee C. B. 1996. Geochemistry of mantle–core differentiation at high pressure. *Nature* 381:686–689.

Li J. and Agee C. B. 2001. The effect of pressure, temperature, oxygen fugacity and composition on partitioning of nickel and cobalt between liquid Fe-Ni-S alloy and liquid silicate: Implications for the Earth's core formation. *Geochimica et Cosmochimica Acta* 65:1821–1832.

Lodders K. 2010. Solar system abundances of the elements. In *Principles and perspectives in cosmochemistry*, edited by Goswami A. and Reddy B. E. Berlin: Springer. pp. 379–417.

Longhi J. 2003. A new view of lunar ferroan anorthosites: Postmagma ocean petrogenesis. *Journal of Geophysical Research* 108:5083.

Longhi J. 2006. Petrogenesis of picritic mare magmas: Constraints on the extent of early lunar differentiation. *Geochemica et Cosmochimica Acta* 70:5919–5934.

Luhr J. F., Carmichael I. S., and Varekamp J. C. 1984. The 1982 eruptions of El Chichón Volcano, Chiapas, Mexico: Mineralogy and petrology of the anhydrite bearing pumices. *Journal of Volcanology and Geothermal Research* 23:69–108.

Malavergne V., Tarrida M., Siebert J., Combes R., Bureau H., and Berthet S. 2006. Partitioning of trace elements between silicate, sulfide and metal at high pressure and high temperature: Investigation of dopant influence on partition behavior (abstract #1288). 37th Lunar and Planetary Science Conference. CD-ROM.

Malavergne V., Brunet F., Righter K., Zanda B., Avril C., Borensztajn S., and Berthet S. 2012. Experimental behavior of sulfur under primitive planetary differentiation processes, the sulfide formations in enstatite meteorites and implications for Mercury (abstract #1860). 43rd Lunar and Planetary Science Conference. CD-ROM.

Mann U., Frost D. J., Rubie D. C., Becker H., and Audétat A. 2012. Partitioning of Ru, Rh, Pd, Re, Ir and Pt between liquid metal and silicate at high pressures and high temperatures-Implications for the origin of highly siderophile element concentrations in the Earth's mantle. *Geochimica et Cosmochimica Acta* 84:593–613.

Martin A. M. and Righter K. 2013. Melting of clinopyroxene+ magnesite in iron-bearing planetary mantles and implications for the Earth and Mars. *Contributions to Mineralogy and Petrology* 166:1067–1098.

McBirney A. R. and Aoki K. 1973. Factors governing the stability of plagioclase at high pressures as shown by spinel-gabbro xenoliths from the Kerguelen Archipelago. *American Mineralogist* 58:271–276.

McDonough W. F. 2003. Compositional model for the Earth's core. *Treatise on Geochemistry* 2:547–568.

Mysen B. O. 1991. Relations between structure, redox equilibria of iron, and properties of magnetic liquids. In *Physical chemistry of magmas*, edited by Perchuk L. L. and Kushiro I. New York: Springer-Verlag. pp. 41–98.

Newsom H. E. 1986. Constraints on the origin of the Moon from the abundance of molybdenum and other siderophile elements. *Origin of the Moon* 1:203–229.

Newsom H. E. and Drake M. J. 1982. The metal content of the eucrite parent body: Constraints from the partitioning behavior of tungsten. *Geochimica et Cosmochimica Acta* 46:2483–2489.

Norman M. D., Borg L. E., Nyquist L. E., and Bogard D. D. 2003. Chronology, geochemistry, and petrology of a ferroan noritic anorthosite clast from Descartes breccia

67215: Clues to the age, origin, structure, and impact history of the lunar crust. *Meteoritics & Planetary Science* 38:645–661.

O'Neill H. S. C. 1991. The origin of the Moon and the early history of the Earth—A chemical model. Part 1: The Moon. *Geochimica et Cosmochimica Acta* 55:1135–1157.

O'Neill H. S. C., Dingwell D. B., Borisov A., Spettel B., and Palme H. 1995. Experimental petrochemistry of some highly siderophile elements at high temperatures, and some implications for core formation and the mantle's early history. *Chemical Geology* 120:255–273.

Palme H. and O'Neill H. S. C. 2003. Cosmochemical estimates of mantle composition. In *The mantle and core*, edited by Holland H. D. and Turekian K. K. Treatise on Geochemistry, vol. 2. pp. 1–38.

Palme H., Spettel B., Wänke H., Bischoff A., and Stöffler D. 1984. Early differentiation of the Moon: Evidence from trace elements in plagioclase. *Journal of Geophysical Research* 89:C3–C15.

Paster T. P., Schauwecker D. S., and Haskin L. A. 1974. The behavior of some trace elements during solidification of the Skaergaard layered series. *Geochimica et Cosmochimica Acta* 38:1549–1577.

Peach C. L. and Mathez E. A. 1993. Sulfide melt-silicate melt distribution coefficients for nickel and iron and implications for the distribution of other chalcophile elements. *Geochimica et Cosmochimica Acta* 57:3013–3021.

Putirka K. D. 2005. Igneous thermometers and barometers based on plagioclase+ liquid equilibria: Tests of some existing models and new calibrations. *American Mineralogist* 90:336–346.

Rai N. and Van Westrenen W. 2014. Lunar core formation: New constraints from metal–silicate partitioning of siderophile elements. *Earth and Planetary Science Letters* 388:343–352.

Ranen M. C. and Jacobsen S. B. 2004. A deep lunar magma ocean based on neodymium, strontium and hafnium isotope mass balance (abstract #1802). 35th Lunar and Planetary Science Conference. CD-ROM.

Righter K. 2002. Does the Moon have a metallic core? Constraints from giant impact modeling and siderophile elements. *Icarus* 158:1–13.

Righter K. 2011. Prediction of metal–silicate partition coefficients for siderophile elements: An update and assessment of PT conditions for metal–silicate equilibrium during accretion of the Earth. *Earth and Planetary Science Letters* 304:158–167.

Righter K. and Drake M. J. 1999. Effect of water on metal-silicate partitioning of siderophile elements: A high pressure and temperature terrestrial magma ocean and core formation. *Earth and Planetary Science Letters* 171:383–399.

Righter K. and Shearer C. K. 2003. Magmatic fractionation of Hf and W: Constraints on the timing of core formation and differentiation in the Moon and Mars. *Geochimica et Cosmochimica Acta* 67:2497–2507.

Righter K., Drake M. J., and Yaxley G. 1997. Prediction of siderophile element metal-silicate partition coefficients to 20 GPa and 2800 C: The effects of pressure, temperature, oxygen fugacity, and silicate and metallic melt compositions. *Physics of the Earth and Planetary Interiors* 100:115–134.

Righter K., Campbell A. J., Humayun M., and Hervig R. L. 2004. Partitioning of Ru, Rh, Pd, Re, Ir, and Au between Cr-bearing spinel, olivine, pyroxene and silicate melts. *Geochimica et Cosmochimica Acta* 68:867–880.

Righter K., Humayun M., and Danielson L. 2008. Partitioning of palladium at high pressures and temperatures during core formation. *Nature Geoscience* 1:321–323.

Righter K., Pando K., and Danielson L. R. 2009. Experimental evidence for sulfur-rich martian magmas: implications for volcanism and surficial sulfur sources. *Earth and Planetary Science Letters* 288:235–243.

Righter K., Pando K. M., Danielson L., and Lee C. T. 2010. Partitioning of Mo, P and other siderophile elements (Cu, Ga, Sn, Ni Co, Cr, Mn, V, and W) between metal and silicate melt as a function of temperature and silicate melt composition. *Earth and Planetary Science Letters* 291:1–9.

Righter K., Danielson L., Pando K., and Lee C. T. 2013. Modelling of equilibrium between mantle and core: Refractory, volatile, and highly siderophile elements (abstract #2358). 44th Lunar and Planetary Science Conference. CD-ROM.

Righter K., Danielson L. R., Pando K., Williams J., Humayun M., Hervig R. L., and Sharp T. G. 2014. Mantle HSE abundances in Mars due to core formation at high pressure and temperature. *Meteoritics & Planetary Science*, doi:10.1111/maps.12393.

Roeder P. L. and Emslie R. 1970. Olivine-liquid equilibrium. *Contributions to Mineralogy and Petrology* 29:275–289.

Seifert S., O'Neill H. S. C., and Brey G. 1988. The partitioning of Fe, Ni and Co between olivine, metal, and basaltic liquid: An experimental and thermodynamic investigation, with application to the composition of the lunar core. *Geochimica et Cosmochimica Acta* 52:603–616.

Shearer C. K. and Righter K. 2003. Behavior of tungsten and hafnium in silicates: A crystal chemical basis for understanding the early evolution of the terrestrial planets. *Geophysical Research Letters* 30:7-1–7-4.

Siebert J., Corgne A., and Ryerson F. J. 2011. Systematics of metal–silicate partitioning for many siderophile elements applied to Earth's core formation. *Geochimica et Cosmochimica Acta* 75:1451–1489.

Smith J. V., Anderson A. T., Newton R. C., Olsen E. J., Crewe A. V., Isaacson M. S., and Wyllie P. J. 1970. Petrologic history of the moon inferred from petrography, mineralogy and petrogenesis of Apollo 11 rocks. Proceedings, 11th Lunar and Planetary Science Conference. pp. 897–925.

Snyder G. A., Taylor L. A., and Neal C. R. 1992. A chemical model for generating the sources of mare basalts: Combined equilibrium and fractional crystallization of the lunar magmasphere. *Geochimica et Cosmochimica Acta* 56:3809–3823.

Solomon S. C. and Longhi J. 1977. Magma oceanography. I-Thermal evolution. Proceedings, 8th Lunar Science Conference. pp. 583–599.

Taura H., Yurimoto H., Kurita K., and Sueno S. 1998. Pressure dependence on partition coefficients for trace elements between olivine and the coexisting melts. *Physics and Chemistry of Minerals* 25:469–484.

Taylor S. R. and Jakes P. 1974. The geochemical evolution of the Moon. Proceedings, 5th Lunar Science Conference. pp. 1287–1305.

Taylor J. R., Wall V. J., and Pownceby M. I. 1992. The calibration and application of accurate redox sensors. *American Mineralogist* 77:284–295.

Thibault Y. and Walter M. J. 1995. The influence of pressure and temperature on the metal-silicate partition coefficients

of nickel and cobalt in a model C1 chondrite and implications for metal segregation in a deep magma ocean. *Geochimica et Cosmochimica Acta* 59:991–1002.
Touboul M., Kleine T., Bourdon B., Palme H., and Wieler R. 2009. Tungsten isotopes in ferroan anorthosites: Implications for the age of the Moon and lifetime of its magma ocean. *Icarus* 199:245–249.
Tuff J., Wood B. J., and Wade J. 2011. The effect of Si on metal–silicate partitioning of siderophile elements and implications for the conditions of core formation. *Geochimica et Cosmochimica Acta* 75:673–690.
Wade J. and Wood B. J. 2005. Core formation and the oxidation state of the Earth. *Earth and Planetary Science Letters* 236:78–95.
Wade J., Wood B. J., and Tuff J. 2012. Metal–silicate partitioning of Mo and W at high pressures and temperatures: Evidence for late accretion of sulphur to the Earth. *Geochimica et Cosmochimica Acta* 85:58–74.
Walker D. and Hays J. F. 1977. Plagioclase flotation and lunar crust formation. *Geology* 5:425–428.
Walker R. J., Horan M. F., Shearer C. K., and Papike J. J. 2004. Low abundances of highly siderophile elements in the lunar mantle: Evidence for prolonged late accretion. *Earth and Planetary Science Letters* 224:399–413.
Walker R. J., McDonough W. F., Honesto J., Chabot N. L., McCoy T. J., Ash R. D., and Bellucci J. J. 2008. Modeling fractional crystallization of group IVB iron meteorites. *Geochimica et Cosmochimica Acta* 72:2198–2216.
Walter M. J. and Thibault Y. 1995. Partitioning of tungsten and molybdenum between metallic liquid and silicate melt. *Science* 270:1186–1189.
Walter M. J., Newsom H. E., Ertel W., and Holzheid A. 2000. Siderophile elements in the Earth and Moon: Metal/silicate partitioning and implications for core formation. *Origin of the Earth and Moon* 1:265–289.
Wänke H., Palme H., Baddenhausen H., Dreibus G., Jagoutz E., Kruse H., Palme C., Spettel B., Teschke F., and Thacker R. 1975. New data on the chemistry of lunar samples—Primary matter in the lunar highlands and the bulk composition of the Moon. Proceedings, 6th Lunar Science Conference. pp. 1313–1340.
Warren P. H. 1990. Lunar anorthosites and the magma-ocean plagioclase-flotation hypothesis: Importance of FeO enrichment in the parent magma. *American Mineralogist* 75:46–58.
Warren P. H., Kallemeyn G. W., and Kyte F. T. 1999. Origin of planetary cores: Evidence from highly siderophile elements in Martian meteorites. *Geochimica et Cosmochimica Acta* 63:2105–2122.
Wetzel D. T., Rutherford M. J., Jacobsen S. D., Hauri E. H., and Saal A. E. 2013. Degassing of reduced carbon from planetary basalts. *Proceedings of the National Academy of Sciences* 110:8010–8013.
Wood J. A., Dickey J. S. Jr., Marvin U. B., and Powell B. N. 1970. Lunar anorthosites and a geophysical model of the moon. Proceedings, 11th Lunar and Planetary Science Conference. pp. 965–988.
Zhang N., Parmentier E. M., and Liang Y. 2013. A 3-D numerical study of the thermal evolution of the Moon after cumulate mantle overturn: The importance of rheology and core solidification. *Journal of Geophysical Research: Planets* 118:1789–1804.

SUPPORTING INFORMATION

Additional supporting information may be found in the online version of this article:

Fig. S1: Clean glass chromatogram.

Fig. S2: Nugget glass chromatogram.

Table S1: Microprobe standards.

Table S2: Microprobe analyses of glass, plagioclase, and olivine in wt%.